Modeling the Earth's Ionosphere by a Phase Screen for the Analysis of Transionospheric SAR Imaging

Mikhail Gilman and Semyon Tsynkov

***Abstract*— In the problems of transionospheric synthetic aperture radar (SAR) imaging, autofocus, and ionospheric tomography, the Earth's ionosphere is often represented by a phase screen. A key advantage of the phase screen is that it reduces the overall dimension of the model. Yet, this convenient simplification comes at a price of introducing inaccuracies into the modeled quantities, such as the phase of the propagating radar signals. In this work, we develop the appropriate metrics to quantify these inaccuracies and evaluate their role for two particular scenarios: SAR imaging through large-scale ionospheric disturbances due to the atmospheric gravity waves (AGWs) and SAR imaging through ionospheric turbulence.**

***Index Terms*— Ionosphere, phase correction, phase screen, synthetic aperture radar (SAR).**

I. Introduction

THE performance of spaceborne synthetic aperture radars (SARs) may be adversely affected by the Earth's ionosphere, especially at low radar frequencies (P-band, UHF, and VHF). If no correction is introduced into the SAR imaging algorithm, the images appear prone to various distortions caused by the propagation of radar signals through the Earth's ionosphere [1], [2], [3], [4], [5], [6], [7], [8], [9].

It is, therefore, important to have the capacity to mitigate the ionospheric distortions of SAR images [10]. In the case of imaging through turbulence, for example, one may use a special autofocus algorithm [11]. In general, the mitigation of image distortions requires that certain ionospheric quantities be known that affect the propagation of electromagnetic waves through the ionospheric plasma. Specifically, this pertains to the electron number density in the ionosphere. To correct the image distortions, the radar needs to reconstruct the electron number density along with pursuing the primary objective of reconstructing the unknown ground reflectivity [10]. (The reconstruction of ionospheric quantities may present an independent task of its own [12], [13], [14], [15], [16].) Accordingly, for the analysis of transionospheric SAR reconstruction, one should have an adequate mathematical model for the electron number density. The electron number density is affected by many physical processes in the ionosphere, including ionization, recombination, and various disturbances, such as the atmospheric gravity waves (AGWs), geomagnetic storms, and ionospheric turbulence [17]. In order to mitigate the distortions in SAR imaging at low radar frequencies, this density should be obtained at the time and place of image acquisition.

The electron number density is a function of three spatial coordinates.[1] As the radar signal propagates through the ionosphere, it builds up a phase advance proportional to the integral of this function along the signal trajectory [10], [18], [19]. Phase screens provide a simplified description of the ionospheric effect on SAR imaging [5], [10], [20], [21]. They replace the gradual accumulation of the phase difference along the signal path with a phase jump at a particular location. Mathematically, a phase screen is a plane positioned at a certain altitude above the Earth's surface with a bivariate function called the screen density defined on this plane. At every location on the screen, the screen density represents the electron number density collapsed vertically and attributed to this location; see Fig. 1. For a signal traveling between the radar antenna on the orbit and target on the ground, the value of the screen density at the intersection point between the signal path (ray) and the screen determines the phase jump for this signal. A typical screen elevation mentioned in the literature is about 350 km, which corresponds to the maximum mean electron number density attained in the F layer of the ionosphere. This choice of the screen elevation is not unique though, and in our recent work [22], we have developed an algorithm of vertical autofocus that positions the screen at the altitude where the ionosphere is most turbulent.

One cannot expect that a 2-D phase screen model will always account exactly for the phase perturbations due to the electron number density, which is a function of three variables. In particular, for all rays that intersect the screen at a certain point, the accumulated phase is assumed the same (accurate to an inessential geometric factor that does not depend on the ionosphere), while for the actual 3-D ionosphere, this may not necessarily be the case. This discrepancy could affect the efficiency of the algorithms that rely on the phase screen assumption, including the autofocus algorithms.

Hence, our goal is to assess the accuracy of modeling the 3-D ionosphere by means of a 2-D phase screen in the case where the primary application is the analysis of transionospheric SAR imaging. We consider two different physical origins of plasma inhomogeneities: first, the traveling ionospheric disturbances (TIDs) due to AGWs, and second, the

Manuscript received 3 June 2023; revised 25 October 2023; accepted 18 November 2023. Date of publication 20 November 2023; date of current version 12 December 2023. This work was supported by the U.S. Air Force Office of Scientific Research (AFOSR) under Grant FA9550-21-1-0086. *(Corresponding author: Mikhail Gilman.)*

The authors are with the Department of Mathematics, North Carolina State University, Raleigh, NC 27695 USA (e-mail: mgilman@ncsu.edu; tsynkov@math.ncsu.edu).

Digital Object Identifier 10.1109/TGRS.2023.3335146

[1]It is also a function of time, but the dependence on time is slow on the scale of an SAR signal round-rip time between the antenna and the target.

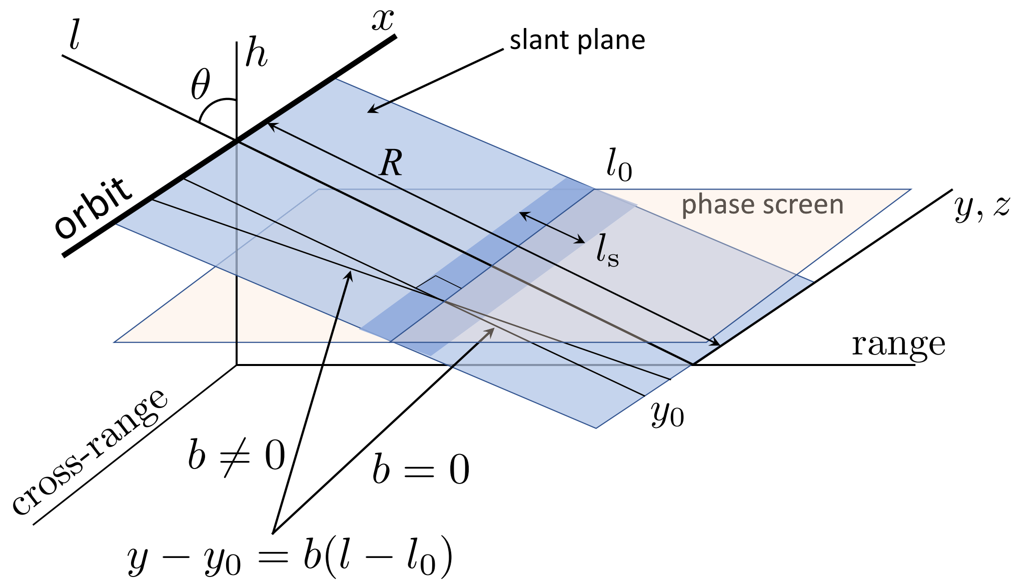

Fig. 1. Imaging geometry: the phase screen (yellow) and slant plane (blue). The highlighted part of the slant plane is within the "thick" ionosphere (not shown); the width of this part is $l_s = h_s / \cos\theta$; see (22).

distortions due to small-scale ionospheric turbulence. In order to characterize the image defocusing for each of these two scenarios, we develop an appropriate accuracy metric and evaluate it for the chosen ionospheric and radar parameters. We use the geometrical optics approximation [10], [18] as the most common approach to describe the propagation of radar signals through the ionosphere. We also limit the analysis to the scalar case and do not consider SAR polarimetry or any effects related to Faraday rotation (see [10], [14], [23], [24], [25], [26], [27], [28], [29], [30]).

Phase perturbations due to dispersive propagation in the inhomogeneous ionosphere may manifest themselves differently on transionospheric SAR images. Image defocusing is the most frequently mentioned effect. It is associated with the fluctuations of the propagation phase (also called scintillations). Other effects include image shifts, fluctuations of image intensity (see [31]), and striping. A cross-range image shift in SAR is usually associated with a perturbation phase that is linear in the cross-range coordinate [10], [27]. A shift by itself might not be considered a distortion, because there is no visual degradation of the image. However, when the coefficient at the linear term varies across the image, the shift becomes coordinate-dependent. Then, it may complicate image coregistration, with a negative impact on SAR interferometry (not analyzed in this work).

Fluctuations of intensity in SAR images, also referred to as amplitude scintillation, should be distinguished from scintillations in the raw signal that passes through the ionosphere. Amplitude scintillation is caused by fluctuations of the ionospheric parameters on the scale of the first Fresnel zone [32]. For a transionospheric radar, the latter is on the order of hundreds of meters and well within the scales of ionospheric turbulence. At the same time, the signal processing involves summation of the signal over the synthetic aperture (SA). Since the length of the SA exceeds the Fresnel radius, the fluctuations in the signal amplitude average out due to the summation [31]. This is the reason why the level of intensity variations in spaceborne SAR images is typically not high, e.g., 2 dB [31]. It is also important to mention that the physical mechanism behind amplitude scintillation is diffraction. Hence, this effect cannot be properly described by geometrical optics, whereas for the phase fluctuations, "the results of geometrical optics method hold beyond the range of its validity" [19].

Arguably, the most prominent manifestation of amplitude scintillation in SAR images is amplitude striping (also called streaking) (see [31], [33], [34]). SAR images obtained after the local sunset in equatorial regions of the Earth exhibit nearly 1-D variations of intensity, with intensity gradient nearly normal to the local meridian. Recent studies have associated this effect with turbulence due to the equatorial plasma bubbles (EPBs) [35], [36], [37]. These ionospheric disturbances are highly anisotropic (essentially 1-D) and aligned with the local magnetic field lines.

The smoothing effect of SA holds true for striping. This is confirmed by the observation that stripes are a lot more prominent in the azimuthal subband images than in full-aperture images (see [35]). At the same time, except near the magnetic poles, the typical sun-synchronous orbits of SAR satellites are generally aligned with the magnetic field and, hence, with perturbations caused by the EPBs. As a result, the entire SA may appear within a single anisotropic Fresnel zone, thus inhibiting the averaging. While striping presents an interesting case of ionospheric distortions, we do not discuss it in this work, in particular when considering the effect of turbulence.

In what follows, Section II introduces the fundamentals of propagation of radar signals through the Earth's ionosphere and SAR imaging, including the concept of eikonal, dispersion of electromagnetic waves in the ionospheric plasma, linearized scattering about the target, and phase screen. Sections III and IV analyze the capacity of the phase screen to accurately represent the effect of a "thick" ionosphere for large-scale and small-scale inhomogeneities, respectively. Section V summarizes the results of the study.

II. Preliminaries

A. Propagation of Radar Signals Through the Earth's Ionosphere

The interrogating signal of an imaging radar is represented as follows:

$$P(t) = A(t)\exp(-i\omega_0 t)$$

where ω_0 is the carrier frequency and $A(t)$ is the envelope. The most common radar waveform is a narrowband pulse. This means that $|d(\ln A)/dt| \ll \omega_0$, and $A(t)$ is compactly supported: $A(t) = 0$ for $|t| > \tau/2$, where $\omega_0\tau \gg 1$.

For the purpose of studying the spaceborne SAR imaging, the Earth's ionosphere can be considered a dilute cold plasma [10, Sec. 3.1]. The propagation of electromagnetic waves in this plasma is subject to temporal dispersion: the phase and group velocities differ from the speed of light c:

$$v_{\text{ph}} \approx c\left(1 + \frac{\omega_{\text{pe}}^2}{2\omega^2}\right), \quad v_{\text{gr}} \approx c\left(1 - \frac{\omega_{\text{pe}}^2}{2\omega^2}\right) \tag{1}$$

where

$$\omega_{\text{pe}}^2 = \frac{4\pi e^2}{m_e} N_e \ll \omega^2 \tag{2}$$

is the electron plasma frequency (also called the Langmuir frequency). In formulas (1) and (2), ω is the signal frequency: $|\omega - \omega_0| \ll \omega_0$, m_e and $-e$ are the electron mass and charge, respectively, and N_e is the electron number density. If the plasma is homogeneous, then the radar signal emitted by the antenna at $\boldsymbol{x}$ and observed at the point $\boldsymbol{z}$ is given by

$$u_{\boldsymbol{x}}(t, \boldsymbol{z}) \approx \frac{\tilde{A}(t - |\boldsymbol{r}|/v_{\text{gr}})}{4\pi|\boldsymbol{r}|}\exp\left(-i\omega_0(t - |\boldsymbol{r}|/v_{\text{ph}})\right) \cdot \Theta(\boldsymbol{r}/|\boldsymbol{r}|) \tag{3}$$

see [10, Sec. 3.2], where $u_{\boldsymbol{x}}$ can be any Cartesian component of the electric field, $\boldsymbol{r} = \boldsymbol{z} - \boldsymbol{x}$, and Θ is the antenna radiation pattern that we drop hereafter. In turn, the notation $\tilde{A}$ in formula (3) pertains to the pulse envelope modified due to the dispersive propagation.[2]

The Earth's ionosphere is inhomogeneous. However, since the radar wavelength is small compared with the scale of inhomogeneities and the frequency is large compared with the electron plasma frequency, one can employ geometrical optics and generalize formula (3) to the case of an inhomogeneous ionosphere as follows (see [10, Sec. 3.3]):

$$u_{\boldsymbol{x}}(t, \boldsymbol{z}) \approx \frac{\tilde{A}(t - T_{\text{gr}})}{4\pi|\boldsymbol{r}|}\exp\left(-i\omega_0(t - T_{\text{ph}})\right) \tag{4}$$

where

$$T_{\text{ph,gr}} \equiv T_{\text{ph,gr}}(\boldsymbol{x}, \boldsymbol{z}) = |\boldsymbol{r}|\int_0^1 \frac{d\xi}{v_{\text{ph,gr}}(\xi)} \tag{5}$$

are the phase/group travel times, and the values of $v_{\text{ph,gr}}(\xi)$ are calculated according to (1) by substituting

$$N_e(\xi) \equiv N_e(\xi; \boldsymbol{x}, \boldsymbol{z}) = N_e\big(\xi\boldsymbol{x} + (1 - \xi)\boldsymbol{z}\big) \tag{6}$$

into formula (2). Formulas (5) and (6) mean that the rays are assumed straight, with the justification provided in [10, Sec. 3.3 and Appendix 4.B].

The quantity cT_{ph} is the eikonal, or phase path of the waves (see [19, Ch. I]). The main effect of the ionosphere on the propagating radar pulse is the perturbation of the free space eikonal $|\boldsymbol{r}|$ that will be denoted by $\varphi(\boldsymbol{x}, \boldsymbol{z})$:

$$\begin{aligned} T_{\text{ph}}(\boldsymbol{x}, \boldsymbol{z}) &\approx \frac{|\boldsymbol{r}| - \varphi(\boldsymbol{x}, \boldsymbol{z})/2}{c} \\ T_{\text{gr}}(\boldsymbol{x}, \boldsymbol{z}) &\approx \frac{|\boldsymbol{r}| + \varphi(\boldsymbol{x}, \boldsymbol{z})/2}{c} \end{aligned} \tag{7}$$

where

$$\varphi(\boldsymbol{x}, \boldsymbol{z}) \approx \frac{4\pi e^2}{m_e\omega_0^2}\underbrace{|\boldsymbol{r}|\int_0^1 N_e(\xi)\,\mathrm{d}\xi}_{\text{STEC}} \tag{8}$$

see [10, Ch. 3]. The underbraced quantity in formula (8) is called the "slant total electron content" (STEC), which is the electron number density integrated over the ray path. Formula (8) shows that the perturbation of the eikonal due to the ionospheric propagation is proportional to STEC.

B. Scattering Model, SAR Imaging, and Mitigation of Distortions

In SAR imaging, one usually employs a linearized scattering model called the first Born approximation [10, Sec. 2.1.1]. In this model, the source of the scattered radiation is the target reflectivity $\nu(\boldsymbol{z})$ multiplied with the impinging field $u_{\boldsymbol{x}}(t, \boldsymbol{z})$ of (4). The scattered field propagates back to the antenna, where it is received and used as data for the reconstruction of $\nu(\boldsymbol{z})$. For free space propagation, the scattered field is given by the Kirchhoff integral

$$u_{\boldsymbol{x}}^{\text{sc}}(t, \boldsymbol{x}) = \int \nu(\boldsymbol{z})\frac{A(t - 2|\boldsymbol{r}|/c)}{4\pi|\boldsymbol{r}|} \cdot \exp\left(-i\omega_0(t - 2|\boldsymbol{r}|/c)\right)\mathrm{d}\boldsymbol{z}. \tag{9}$$

The imaging is performed by compensating the two-way propagation delay $2|\boldsymbol{r}|/c$ for a set of consecutive antenna locations $\{\boldsymbol{x}_j\}_{j=1}^N$ that are spread over the SA and called the synthetic array. This procedure is referred to as matched filtering (see [10], [38], [39]). Specifically, for the received field given by (9), we use the following formula to build the image $I(\boldsymbol{y})$ that approximates the unknown reflectivity $\nu(\boldsymbol{z})$:

$$I(\boldsymbol{y}) = \frac{1}{N}\sum_{j=1}^N \int u_{\boldsymbol{x}_j}^{\text{sc}}(t, \boldsymbol{x}_j)\overline{A(t - 2|\boldsymbol{r}'_j|/c)} \cdot \exp\left(i\omega_0(t - 2|\boldsymbol{r}'_j|/c)\right)\mathrm{d}t. \tag{10}$$

In (10), $\boldsymbol{r}'_j = \boldsymbol{y} - \boldsymbol{x}_j$, and the summation is conducted over the synthetic array that corresponds to the location $\boldsymbol{y}$ (see Section II-C for the specific details on imaging geometry).

In the case of imaging through the ionosphere, we take into account the dispersive propagation (4). Expression (9) for the received field is modified accordingly:

$$u_{\boldsymbol{x}}^{\text{sc}}(t, \boldsymbol{x}) = \int \nu(\boldsymbol{z})\frac{\tilde{A}(t - 2T_{\text{gr}}(\boldsymbol{x}_j, \boldsymbol{z}))}{4\pi|\boldsymbol{r}|} \cdot \exp\left(-i\omega_0(t - 2T_{\text{ph}}(\boldsymbol{x}_j, \boldsymbol{z}))\right)\mathrm{d}\boldsymbol{z} \tag{11}$$

[2]For a linear frequency modulated signal (chirp), the modification $\tilde{A}(t)$ includes changes in the chirp rate and duration. These changes depend on the total electron content given by (8) (see [10, Sec. 3.2]).

and the inversion formula (10) becomes

$$I(\boldsymbol{y}) = \frac{1}{N}\sum_{j=1}^{N}\int u^{\mathrm{sc}}_{\boldsymbol{x}_j}(t,\boldsymbol{x}_j)\overline{\tilde{A}(t-2T_{\mathrm{gr}}(\boldsymbol{x}_j,\boldsymbol{y}))} \cdot \exp\left(i\omega_0(t-2T_{\mathrm{ph}}(\boldsymbol{x}_j,\boldsymbol{y}))\right)\mathrm{d}t. \quad (12)$$

While the received field (11) represents the data for inversion, the actual inversion (12) requires the travel times $T_{\mathrm{ph,gr}}(\boldsymbol{x}_j,\boldsymbol{y})$ of (5) and modified envelope $\tilde{A}$. Hence, we have to know the values of STEC for all signal paths between the antenna locations $\boldsymbol{x}_j$ and image points $\boldsymbol{y}$; see (6)–(8). Thus, to build a 2-D image, we should know the values of N_e in a 3-D domain between the orbit and the target.

In our earlier work [1], [40] (see also [10]), we have shown that SAR imaging on two distinct carrier frequencies allows one to reconstruct the unknown STEC and subsequently correct the image distortions in the case of a nonturbulent ionosphere. In general, the algorithms for the retrieval of ionospheric quantities (see [12], [27], [28], [41]) may rely on certain assumptions about the target [e.g., that it contains isolated point scatterers $\nu_k\delta(\boldsymbol{z}-\boldsymbol{z}_k)$] and/or redundancy of the data. Often, a low-dimensional parametrization of the electron number density (or STEC) is employed. The phase screen introduced in Section II-E offers precisely that—a convenient way of reducing the overall dimension of the model. Our objective is to analyze the implications for the accuracy of modeling associated with this dimension reduction.

C. Imaging in the Slant Plane and the Phase Screen

Consider the imaging geometry illustrated in Fig. 1. With the help of range compression [22], we reduce the full SAR imaging formulation to a formulation that involves only one target coordinate, the cross range (also called azimuth). This formulation proves sufficient for analyzing the effect of the phase screen. Hence, we conduct the analysis in the "slant plane" hereafter, with z and y being the cross-range coordinate of the scatterer and image points, respectively. We will also use l as the slant coordinate that is related to elevation h as $h = l\cos\theta$, where θ is the incidence angle, i.e., the angle between the slant plane and the vertical direction. We assume that a "thick" ionosphere is specified by means of a bivariate electron number density that depends on the azimuth and altitude: $N_e = N_e(z,h)$, but does not explicitly depend on the range as an independent coordinate. The phase screen density will then become a univariate function (see Section II-E).

Different rays passing through a given point (z_0,l_0) on the slant plane will be parameterized by the squint parameter b:

$$\mathrm{RaySgmnt}(b) \equiv \mathrm{RaySgmnt}(b;z_0,l_0) \stackrel{\mathrm{def}}{=} \left\{(z,l)\,\middle|\, \frac{z-z_0}{l-l_0} = b = \mathrm{const}, 0\le l\le R\right\} \quad (13)$$

where R is the distance between the antenna track and the target area; see Fig. 1. We use the same constant b to parametrize the STEC, see (8), for the corresponding rays:

$$\mathrm{STEC}(b;z_0,l_0) = \int_{\mathrm{RaySgmnt}(b;z_0,l_0)} N_e(z,h)\,\mathrm{d}\ell \quad (14)$$

where $\mathrm{d}\ell$ is the path length differential. Comparing (14) with (8), we see that

$$\varphi(\boldsymbol{x},\boldsymbol{z}) = \frac{4\pi e^2}{m_e\omega_0^2}\mathrm{STEC}(b;z_0,l_0) \quad (15)$$

where the points $\boldsymbol{x}$ and $\boldsymbol{z}$ belong to the ray defined by (13) on the chosen slant plane.

Hereafter, we assume that the target is approximately at the broadside of the antenna, and the size of the target, as well as that of the SA, is much smaller than the distance R; see Fig. 1. Then

$$|\boldsymbol{x}-\boldsymbol{z}| \approx R + \frac{(x-z)^2}{2R} \quad (16)$$

where x is the azimuthal position of the antenna. The procedure of range compression described in [22] allows one to extract and, subsequently, drop the time-dependent terms in (9)–(12) after formula (16) has been used for distances. The resulting expression for the image in (12) takes the form

$$I(y) = \int \nu(z)W(y,z)\,\mathrm{d}z$$

where the integral with no limits is taken over $\mathbb{R}$ and the kernel $W(y,z)$ is given by

$$W(y,z) = \frac{1}{N}\sum_{x_j\in\mathrm{SA}(y)\cap\mathrm{SA}(z)} \exp\left[2ik\frac{y-z}{R}\left(x_j - \frac{y+z}{2}\right)\right] \times\exp\left[-ik\left(\varphi(x_j,z)-\varphi^{\mathrm{rec}}(x_j,y)\right)\right]. \quad (17)$$

In (17), $k = \omega_0/c$ is the carrier wavenumber, φ is the perturbation of the eikonal (7) and (8) that depends only on the azimuthal coordinates x and z in accordance with (13)–(15), and φ^{rec} is introduced with the purpose of mitigating the distortions due to the ionospheric turbulence. The summation range in (17) is given by the overlap of two SAs, $\mathrm{SA}(y)$ and $\mathrm{SA}(z)$, centered at y and z, respectively,

$$\mathrm{SA}(y) = \{x \,|\, |x-y| \le L_{\mathrm{SA}}/2\}$$
$$\mathrm{SA}(z) = \{x \,|\, |x-z| \le L_{\mathrm{SA}}/2\}. \quad (18)$$

The quantity L_{SA} in (18) is the length of the SA. It is an important parameter that determines the resolution and sensitivity to phase distortions, as we shall see later. The choice of L_{SA} is discussed, e.g., in [10, Ch. 2].

Without the second exponential, formula (17) yields the unperturbed imaging kernel

$$W_0(y,z) \approx \mathrm{sinc}\left(kL_{\mathrm{SA}}\frac{y-z}{R}\right) \quad (19)$$

where $\mathrm{sinc}(x) \stackrel{\mathrm{def}}{=} \sin(x)/x$. This kernel is also called the point spread function (PSF), because it can be considered as an image of a point scatterer $\nu(z') = \delta(z'-z)$. We will define the azimuthal resolution Δ_A as the semiwidth of the main lobe of the PSF:

$$\Delta_A = \frac{\pi R}{kL_{\mathrm{SA}}}. \quad (20)$$

The true meaning of the correction term φ^{rec} in formula (17) is perturbation of the eikonal along the ray path between $\boldsymbol{x}_j$ and $\boldsymbol{y}$. Our goal, however, is to assess how accurately an infinitesimally thin phase screen can approximate the phase perturbations accumulated over a finite propagation distance. Therefore, in our subsequent analysis, we will adhere to the scenario where the actual perturbation $\varphi(x, z)$ is considered due to the signal propagation in an ionosphere of a finite thickness, see (5)–(8), while the reconstruction $\varphi^{\text{rec}}(x, y)$ is implemented via a phase screen. In turn, the phase screen is realized by means of a fixed scalar $\xi \sim 0.5$ and fixed univariate function $\varphi_S(\cdot)$, such that [see (6)]

$$\varphi^{\text{rec}}(x, y) = Q\varphi_S\big(\xi x + (1-\xi)y\big). \tag{21}$$

The geometric factor $Q = (1 + b^2)^{1/2}$ in (21) does not depend on N_e and b is given by (13). The interpretation of Q is further discussed after (28).

D. Spatial and Temporal Scales of the Ionosphere and the Horizontal Scales of Inhomogeneities

A commonly used formulation for the vertical distribution of the ionospheric electron number density, called the Chapman profile (see [42], [43]), involves three parameters: $\mathcal{N}$, h_m, and h_s, to define the ionospheric electron number density $N_e(h)$ as a function of the elevation h as follows:

$$\begin{aligned} N_e(h) &= \mathcal{N} e^{a(1-z-e^{-z})}, \quad \text{where } a \in \{0.5, 1\} \\ z &= \frac{h - h_m}{h_s}. \end{aligned} \tag{22}$$

In formula (22), $\mathcal{N} = \text{const}$ is the maximum density, h_m is the mean elevation of a given ionospheric layer, h_s is its thickness, $a = 0.5$ for the E layer, and $a = 1$ for the F1 and F2 layers [42, Sec. III]. The values of h_m and h_s for the F2 layer are equal to 350 and 50 km, respectively, according to [42], whereas [43] gives $h_s \sim 200$ km for the "slab thickness," i.e., the thickness of the ionosphere as a whole.

We will use the spatial parameters of the Chapman profile (22), namely, h_m and h_s, to characterize the effects due to a finite thickness of the ionosphere. Assume that the phase screen elevation is close to h_m, so that the main contribution to the integral in (14) comes from the interval of length $l_s = h_s/\cos\theta$ centered around the point where the ray intersects the phase screen; see Fig. 1 (the corresponding part of the slant plane is highlighted). For the rays connecting a given point on the phase screen and all antenna positions within a synthetic array of length L_{SA}, let d be the maximum possible distance *in the cross-range direction* between the points within the highlighted area in Fig. 1. Obviously

$$d \sim L_{\text{SA}} \frac{h_s}{H} \tag{23}$$

where H is the orbit elevation. For example, with the lower estimate for h_s, i.e., $h_s \sim 50$ km, $L_{\text{SA}} = 50$ km, and orbit elevation $H = 500$ km used in [10], formula (23) yields

$$d = L_{\text{SA}} \frac{h_s}{H} = \frac{h_s}{10} \sim 5 \text{ km}. \tag{24}$$

The case where the ionosphere can be linearized on the scale of d (i.e., approximated with sufficient accuracy by the first two terms of the Taylor expansion) will be called the large-scale case. In the opposite case that will be referred to as small scale, we assume that linearization is valid only for much shorter scales, up to $d_* \ll d$.

Consider a common type of perturbations of the ionosphere known as the TIDs, which are a manifestation of the AGWs [44]. For large-scale AGWs/TIDs, the characteristic spatial and temporal scales are $\gtrsim$1000 km and 0.5–3 h, respectively, whereas for medium-scale AGWs/TIDs, those are 100–1000 km and 0.15–1 h (see [44, Sec. 1]). Both spatial scales exceed (24) by at least two orders of magnitude. Hence, the effect of AGWs/TIDs can be analyzed using Taylor's expansion of the ionospheric parameters (see Section III).

On the other hand, the value given by (24) is too large for a comprehensive description of the ionospheric turbulence where scales down to 70 m are observed [45], [46]. This is a small-scale case, and we will not employ Taylor's representation with respect to the horizontal coordinates when we analyze the effect of ionospheric turbulence (see Section IV).

E. Electron Number Density and Phase Screen Density

In the slant plane shown in Fig. 1, the coordinates are azimuth and slant range. Accordingly, the screen density in this plane becomes the function of a single auxiliary variable s. Specifically, consider a ray between the point (x, R) on the orbit and point $(z, 0)$ on the ground, where both points belong to the slant plane shown in Fig. 1. This ray intersects the phase screen at the point (s, l), where in agreement with (6) and (21)

$$s = \xi x + (1-\xi)z, \quad l = \xi R. \tag{25}$$

We define $\varphi_S(s)$ of (21), the phase screen density at this point, as the perturbation of the eikonal in formula (7) for a ray passing through this point and having $b = 0$ (i.e., $x = z$). We see that φ_S is related to the special case of STEC in (14) that corresponds to $b = 0$. The latter quantity will be called the "broadside TEC" (BTEC)

$$\begin{aligned} \text{BTEC}(s) &= \int_{\text{RaySgmnt}(0;s,0)} N_e\big(s, h\big)\, d\ell \\ &= \frac{1}{\cos\theta}\int_0^H N_e\big(s, h\big)\, dh = \frac{1}{\cos\theta}\text{TEC}(s) \end{aligned} \tag{26}$$

so that

$$\varphi_S(s) = \frac{4\pi e^2}{m_e\omega_0^2}\text{BTEC}(s) \tag{27}$$

see (8) and (15). In formula (26), θ is the incidence angle; see Fig. 1, and TEC is the vertical total electron content, which is the quantity often used in geomagnetic research and ionospheric models (see [10], [17], [47]).[3] Alternatively, we can think of a very thin layer of plasma at the elevation $h = \xi H$, such that the product of its thickness $d^{(\text{thin})}$ and electron number density $N_e^{(\text{thin})}(s, h) \equiv N_e^{(\text{thin})}(s)$ is finite:

$$N_e^{(\text{thin})}(s) \cdot h_s^{(\text{thin})} = \text{TEC}(s). \tag{28}$$

[3]There are a few caveats about using a model- or measurement-derived TEC in (26). First, the orbits of all known SAR satellites are within the ionosphere, though the bulk of it is still between the orbit and the ground [17]. Besides, the last equality in (26) assumes that the ionosphere is homogeneous in the range direction (see Section II-C). In this work, we use the available values of the TEC to obtain rough estimates of the quantities/phenomena of interest.

The representation (28) is helpful in clarifying the meaning of the geometric factor Q in (21): for a ray defined by the squint parameter b, the value of Q is the length of the segment inside the layer relative to that for the broadside ray (i.e., with $b = 0$).

Note that the phase jump due to a single crossing of the phase screen is $\omega_0 \cdot (1/2)(\varphi_S/c) = \pi\varphi_S/\lambda_0$, whereas the phase advance and group delay in the received field are twice that [see (7) and (12)] due to the round-trip propagation.

III. Large-Scale Variations of Ionospheric Parameters

Here, we will consider phase perturbations due to large-scale TIDs, as specified in Section II-D. The smallest horizontal scale L_{TID} for the events of this type is still much larger than most of the other relevant length scales:

$$\frac{h_s}{L_{\mathrm{TID}}} \lesssim \frac{1}{3}, \quad \frac{h_m}{L_{\mathrm{TID}}} \lesssim \frac{1}{3}, \quad \frac{L_{\mathrm{SA}}}{L_{\mathrm{TID}}} \lesssim \frac{1}{20}. \tag{29}$$

This allows us to use the Maclaurin expansion with respect to the horizontal coordinate for the electron number density as follows:

$$N_e(s,h) = N_0(h) + N_1(h)s + N_2(h)s^2 + N_3(h)s^3. \tag{30}$$

We assume that this expansion is valid for $|s| \le L_{\mathrm{SA}}$, because $L_{\mathrm{SA}} \ll L_{\mathrm{TID}}$; see (29).

We will consider the imaging kernel (17) for a certain fixed value of z. We see that $|W| \sim 1$ can be achieved only if both exponentials are not oscillating with j over the synthetic array. Note that the first exponential is oscillating when $|y - z| \gg \Delta_A$, where Δ_A is the azimuthal resolution; see (20). This results in $|W| \ll 1$.[4] At the same time, for $|y - z| \lesssim \Delta_A$, the expression for the second exponent can be simplified as

$$\varphi(x_j, z) - \varphi^{\mathrm{rec}}(x_j, y) \approx \varphi(x_j, z) - \varphi^{\mathrm{rec}}(x_j, z) \tag{31}$$

because $\Delta_A \ll L_{\mathrm{TID}}$.

Let $|z| \le L_{\mathrm{SA}}/2$, and suppose that the segment $\mathrm{RaySgmnt}_S(z,b) \overset{\mathrm{def}}{=} \mathrm{RaySgmnt}(b; z, 0)$ connects the points (x_j, R) and $(z, 0)$; see (13). It intersects the phase screen at the point $(z + \mathcal{B}\xi H, \xi H)$, where $\mathcal{B} = b/\cos\theta$. Next, consider the ray segment with $b = 0$ that passes through the same phase screen point, i.e., $\mathrm{RaySgmnt}_B(z,b) \overset{\mathrm{def}}{=} \mathrm{RaySgmnt}(0; z + \mathcal{B}\xi H, 0)$. Then, in formula (31), the quantities $\varphi(x_j, z)$ and $\varphi^{\mathrm{rec}}(x_j, z)$ are obtained by integrating the electron number density over $\mathrm{RaySgmnt}_S(z,b)$ and $\mathrm{RaySgmnt}_B(z,b)$, respectively (see Section II-E), where

$$x_j = z + \mathcal{B}H. \tag{32}$$

Let us define a new function U as follows:

$$U(z,b) = \cos\theta \left(\frac{\mathrm{STEC}\big(\mathrm{RaySgmnt}_S(z,b)\big)}{\sqrt{1+b^2}} - \mathrm{BTEC}\big(\mathrm{RaySgmnt}_B(z,b)\big) \right) \tag{33}$$

so that

$$k\big(\varphi(x_j,z) - \varphi^{\mathrm{rec}}(x_j,z)\big) = k\frac{4\pi e^2}{m_e\omega_0^2}\frac{\sqrt{1+b^2}}{\cos\theta}U(z,b). \tag{34}$$

Formulas (33) and (34) characterize the accuracy of representation of a "thick" ionosphere by means of a phase screen.

By substituting (34) with (31) into (17), we can describe the distortions of the image as compared with the perturbation-free case described by the kernel (19). First, using the expansion (30) in (8), we obtain

$$\begin{aligned} U(z,b) = \int \Big(& \mathcal{B}N_1(h)(h - \xi H) \\ & + N_2(h)\big[(z + \mathcal{B}h)^2 - (z + \mathcal{B}\xi H)^2\big] \\ & + N_3(h)\big[(z + \mathcal{B}h)^3 - (z + \mathcal{B}\xi H)^3\big] \Big)\, \mathrm{d}h. \end{aligned} \tag{35}$$

Different powers of $\mathcal{B}$ in (35) result in different types of distortions of the imaging kernel. Introduce

$$\begin{aligned} \mathcal{U}_1 &= \int N_1(h)(h - \xi H)\, \mathrm{d}h \\ \mathcal{U}_{21} &= \int N_2(h)(h - \xi H)\, \mathrm{d}h \\ \mathcal{U}_{22} &= \int N_2(h)\big(h^2 - (\xi H)^2\big)\, \mathrm{d}h \\ \mathcal{U}_3 &= \int N_3(h)\big(h^3 - (\xi H)^3\big)\, \mathrm{d}h. \end{aligned} \tag{36}$$

Then, using (32), we identify a phase term in (17) that is linear in x_j:

$$\begin{aligned} &\underbrace{2k\frac{y-z}{R}\left(x_j - \frac{y+z}{2}\right)}_{\text{baseline phase}} - \underbrace{k\big(\varphi(x_j,z) - \varphi^{\mathrm{rec}}(x_j,y)\big)}_{\text{“thick” ionosphere and a phase screen}} \\ &\downarrow \\ &2k\frac{y-z}{R}x_j - Cx_j + \mathrm{const}(x_j) \end{aligned} \tag{37}$$

where

$$C = k\frac{\sqrt{1+b^2}}{\cos\theta}\frac{4\pi e^2}{m_e\omega_0^2}\left[\mathcal{U}_1 + 2z\left(\mathcal{U}_{21} - \frac{1}{H\cos\theta}\mathcal{U}_{22}\right)\right].$$

When substituted into (17), the term Cx_j in (37) yields a shift of the image in the cross-range direction. This can be explained by associating the peak of $W_0(y,z) \equiv W_0(y - z)$ at $y = z$ in (19) with the $(y - z)$ factor in the baseline phase term in (37), i.e., the first complex exponent in (17). The expression in the bottom line of (37) can be transformed as follows:

$$2k\frac{y-z}{R}x_j - Cx_j = 2k\frac{y - (z + z_C)}{R}x_j \tag{38}$$

where

$$\begin{aligned} z_C = \frac{CR}{2k} = & \frac{\sqrt{1+b^2}}{2\cos^2\theta}\frac{4\pi e^2}{m_e\omega_0^2} \\ & \cdot \left[\mathcal{U}_1 + 2z\left(\mathcal{U}_{21} - \frac{1}{H\cos\theta}\mathcal{U}_{22}\right)\right] \end{aligned} \tag{39}$$

see [10, Sec. 3.9.1]. Accordingly, the scatterer coordinate z in the formula $W_0(y,z) = \mathrm{sinc}\big(\pi(y-z)/\Delta_A\big)$, see (19) and (20), is replaced with $z + z_C$. For example, when the target is a single

[4] A notable exception is the case where the perturbation phase is linear in x; see (38) and (39).

point scatterer, i.e., $\nu(z') = \nu_0\delta(z'-z)$, and all higher order distortions can be neglected, then the resulting image, accurate to a phase factor, will be given by $I(y) \propto W_0(y, z+z_C)$, and hence, the maximum amplitude will be at $y = z + z_C$.

The part of z_C proportional to $\mathcal{U}_1$ shifts the SAR image as a whole. While technically a distortion, such a shift does not result in a visual degradation of the image, e.g., smearing or broadening of the peaks, increase of SNR, or shape deformations [2].

Next, we identify the leading coordinate-dependent term proportional to $\mathcal{B}$, as well as the leading terms $\propto \mathcal{B}^2$ and $\propto \mathcal{B}^3$ on the right-hand side of (35) as follows:

$$\begin{aligned} U_{21} &= 2\mathcal{B}z\left(\mathcal{U}_{21} - \frac{1}{H\cos\theta}\mathcal{U}_{22}\right) \\ U_{22} &= \mathcal{B}^2 \cdot \mathcal{U}_{22} \\ U_3 &= \mathcal{B}^3 \cdot \mathcal{U}_3. \end{aligned} \tag{40}$$

In (40), we have assumed that $|N_3 z| \ll |N_2|$, because $|z| \le L_{\mathrm{SA}}/2$; see (30). The term U_{21} given by (40) yields a cross-range shift of the image that depends on the cross-range coordinate z; see (39). Hence, it amounts to a geometric distortion. The term U_{22} evaluated at $\max|\mathcal{B}| = L_{\mathrm{SA}}/(2R\cos\theta)$ yields the quadratic phase error (QPE) that characterizes the smearing of the central lobe of the PSF, while U_3 leads to the cubic phase error (CPE) that is responsible for the asymmetry of the PSF sidelobes (see [10], [48], [49], [50]).

To get an idea of the magnitude of the distortions given by (39) and (40), we will evaluate them for an event illustrated by [51, Fig. 3 (top-left panel)], where the maximum value of N_e changed from $N_e^{\mathrm{init}} \approx 7\times 10^{11}$ m^{-3} to $N_e^{\mathrm{final}} \approx 5 \times 10^{11}$ m^{-3} in about 2 h, with the vertical TEC of about 10 TECU $\equiv 10\times 10^{16}$ m^{-2}. Since the data in [51] do not provide the spatial scales directly, we identify this event as a large-scale TID from its temporal scale; see Section II-D, and assume the lower bound for the spatial scale of this kind of TID, i.e., $L_{\mathrm{TID}} = 10^3$ km. To obtain a rough estimate, we use STEC $\sim$ TEC$/\cos\theta$ (see footnote 3), and assume that the variable part of the electron number density associated with the TID behaves as follows:

$$N_i(s,h) \approx \begin{cases} \mathcal{N}_i(s), & |h-h_m| \le h_s/2 \\ 0, & \text{otherwise} \end{cases}$$

where $i = 0$–3. In order to estimate the coefficients in the expansion (30), we define $\mathcal{N}_0$ as $|N_e^{\mathrm{final}} - N_e^{\mathrm{init}}| \sim 2\times 10^{11}$ m^{-3} and assume a constant homogeneous background of $\mathcal{N}_B = (N_e^{\mathrm{final}} + N_e^{\mathrm{init}})/2 \sim 6\times 10^{11}$ m^{-3}, so that $\mathcal{N}_0/\mathcal{N}_B = 1/3$. Accordingly

$$\begin{aligned} \mathcal{N}_1 &= \frac{\partial N_e}{\partial s} \sim \frac{\mathcal{N}_0}{L_{\mathrm{TID}}} \\ \mathcal{N}_2 &= \frac{1}{2}\frac{\partial^2 N_e}{\partial s^2} \sim \frac{1}{2}\frac{\mathcal{N}_0}{L_{\mathrm{TID}}^2} \\ \mathcal{N}_3 &= \frac{1}{6}\frac{\partial^3 N_e}{\partial s^3} \sim \frac{1}{6}\frac{\mathcal{N}_0}{L_{\mathrm{TID}}^3}. \end{aligned} \tag{41}$$

Then, taking $h_m \approx \xi H$, we obtain the following upper bounds for the integrals in (36):

$$\begin{aligned} |\mathcal{U}_{21}| &\le \mathcal{N}_2 \cdot \frac{h_s}{2} \cdot h_s \\ |\mathcal{U}_{22}| &\le \mathcal{N}_2 \cdot \left[\left(\xi H + \frac{h_s}{2}\right)^2 - (\xi H)^2\right] \cdot h_s \\ |\mathcal{U}_3| &\le \mathcal{N}_3 \cdot \left[\left(\xi H + \frac{h_s}{2}\right)^3 - (\xi H)^3\right] \cdot h_s. \end{aligned} \tag{42}$$

In turn, substituting $h_s = 200$ km and $h_m = \xi H = 350$ km into (42), we can estimate the left-hand sides in (40) as follows:

$$\begin{aligned} |U_{21}| &\lesssim \frac{4}{7}|\mathcal{B}z| \cdot \mathcal{N}_2 h_s h_m \\ |U_{22}| &\lesssim \frac{2}{3}\mathcal{B}^2 \cdot \mathcal{N}_2 h_s h_m^2 \\ |U_3| &\lesssim |\mathcal{B}|^3 \cdot \mathcal{N}_3 h_s h_m^3. \end{aligned} \tag{43}$$

We will use the same radar parameters as in [10, Table 1.1], in particular, $\omega_0 = 300$ MHz, $L_{\mathrm{SA}} = 5\times 10^4$ m, $R = 10^6$ m, and $\cos\theta = 1/2$. Combining (29), (34), (41), and (43), we arrive at the following estimates:

$$\left|\frac{\partial z_C}{\partial z}\right| \lesssim 5\times 10^{-5}, \quad \mathrm{QPE} \lesssim 0.2, \;\; \mathrm{CPE} \lesssim 10^{-3}.$$

The resulting distortions are small. In particular, it is noted in [49] that the PSF "degrades very little for phase errors less than $\pi/4$." Moreover, one can always choose ξ so as to cancel at least one of the integrals in (36), thus zeroing out the leading term of the associated distortion.

Altogether we conclude that in the case of large-scale AGWs/TIDs, the corrections of ionospheric phase perturbations of SAR signals can be accurately represented using a phase screen.

IV. Ionospheric Turbulence

Imaging through a turbulent ionosphere is often considered in the stochastic framework (see [10, Ch. 4] and the references therein). We will use the following model for the electron number density in the turbulent ionosphere:

$$N_T(\boldsymbol{s}) = N_e(\boldsymbol{s}) + \mu(\boldsymbol{s}), \quad \text{where } \langle\mu\rangle = 0. \tag{44}$$

In (44), $\boldsymbol{s}$ is a point on the slant plane, N_e and μ denote the baseline (or averaged) and turbulent part of the total density N_T, respectively, and $\langle\cdot\rangle$ means statistical averaging. The intensity of turbulent fluctuations will be denoted by $\langle\mu^2\rangle$ and can be determined from the available ionospheric models (see [52]). Alternatively, we can evaluate $\langle\mu^2\rangle$ via

$$M = \frac{\sqrt{\langle\mu^2\rangle}}{N_e} \tag{45}$$

where M is considered a constant with the value between 5×10^{-3} and 10^{-1} (see [4]).

Introduce

$$v_{\mathrm{ph}}(N_T; z, l) \quad \text{and } v_{\mathrm{ph}}(N_e; z, l)$$

by substituting $N_T(z,l)$ and $N_e(z,l)$ into formulas (1) and (2). To represent the difference between the turbulent and baseline eikonals over the same ray, it is convenient to use

$$\beta(z,l) \stackrel{\text{def}}{=} \frac{c}{v_{\text{ph}}(N_T;z,l)} - \frac{c}{v_{\text{ph}}(N_e;z,l)}. \tag{46}$$

Since, in addition to the inequality in (2), we have $M \ll 1$ [4], formulas (1) and (46) yield

$$\beta(z,l) \approx \frac{4\pi e^2}{m_e\omega_0^2}\mu(z,l).$$

According to (44), we replace formula (8) with

$$\varphi = \varphi_{N_e} + \varphi_\mu \equiv \varphi_{N_e} + \int_{\text{RaySgmnt}} \beta(z,l)\,d\ell$$

where φ_{N_e} is the perturbation of the eikonal due to N_e, i.e., the baseline part of the ionospheric electron number density. We will assume that the spatial scale of N_e is such that φ_{N_e} can be compensated efficiently by the phase screen; see Section III. For this reason, we exclude φ_{N_e} from further consideration by redefining

$$\varphi = \int_{\text{RaySgmnt}} \beta(z,l)\,d\ell. \tag{47}$$

Similarly to Section III, we will reduce the number of independent variables in the second exponent $\varphi(x,z) - \varphi^{\text{rec}}(x,y)$ on the right-hand side of (17). As long as we are interested in having $|W| \sim 1$ rather than $|W| \ll 1$, i.e., $|y-z| \lesssim \Delta_A$ [see (31)], we can replace the second exponent in (17) with a bivariate function ϕ as follows:

$$\begin{gathered}\varphi(x_j,z) - \varphi^{\text{rec}}(x_j,y)\\ \downarrow \\ \varphi(x_j,y) - \varphi^{\text{rec}}(x_j,y) = \phi(x_j,y).\end{gathered} \tag{48}$$

Note that a similar reduction offered by (31) is possible, because $\Delta_A \ll L_{\text{TID}}$. In this section, we are considering much shorter spatial scales than L_{TID} in Section III. Yet, the simplification in (48) is legitimate, because the azimuthal resolution of modern spaceborne SAR systems is $\lesssim$10 m, whereas the smallest spatial scales of the variation of $\varphi(\cdot,z)$ are on the order of the correlation length of the medium (see [10, Appendix 4A]). A lower bound for this correlation length is the inner scale of ionospheric turbulence. In turn, the value of 70 m reported in [45] and [46] is indicative of the latter (see Section II-D).

The analysis of SAR imaging through a turbulent ionosphere that we conducted in [2] and [10, Ch. 4] aimed specifically at quantifying the distortions of spaceborne SAR images. In that study, the following two parameters have been identified as most important for image quality (see [10, Table 1.2]).

1) Correlation length of the eikonal relative to the length of the SA.
2) Variance of the propagation phase expressed as follows:

$$\mathcal{D}^2 = k^2\langle\varphi^2\rangle/2. \tag{49}$$

Moreover, we have shown in [10, Ch. 4] that the dependence of $\langle\varphi^2\rangle$ on the azimuthal coordinate is weak, and consequently, one can assume $\langle\varphi^2\rangle \approx$ const. Yet, we will see that this assumption does not always hold for $\langle\phi^2\rangle$, where ϕ is introduced in (48). In the rest of this section, we extend the analysis of [10, Ch. 4] to the case represented by (17) and (21). In other words, we proceed beyond the plain quantification of image distortions due to a turbulent ionosphere and implement the phase corrections using a phase screen.

A. Statistics of Eikonals for the Rays Passing Through a Single Phase Screen Point

1) General Formulation and the Geometry of Rays: Consider RaySgmnt$(b;z_0,l_0)$, see (13), for a certain point (z_0,l_0) on the phase screen. This ray probes the electron number density N_T at the points that depend on the squint parameter b, whereas the value of φ_S in (21) corresponds to the broadside eikonal; see also (27). The latter means that φ^{rec} does not depend on N_T beyond the ray with $b=0$. To quantify the difference between the actual eikonals and those modeled by the phase screen as in (21), we will use the following metric:

$$\zeta_{\tilde\varphi}(b) = \frac{1}{2}\frac{S_{\tilde\varphi}(b)}{\langle\tilde\varphi^2(0)\rangle} = \frac{1}{2}\frac{\langle|\tilde\varphi(b)-\tilde\varphi(0)|^2\rangle}{\langle\tilde\varphi^2(0)\rangle}. \tag{50}$$

In (50), $\tilde\varphi(b)$ is the perturbation of the eikonal (47) normalized by the factor $Q = (1+b^2)^{1/2}$ [see (21)]:

$$\begin{aligned}\tilde\varphi(b) &= \frac{1}{Q}\varphi(b) = \frac{1}{Q}\int_{\text{RaySgmnt}(b;z_0,l_0)} \beta(z,l)\,d\ell\\ &= \int \beta\big(z(l,b),l\big)\,dl\end{aligned} \tag{51}$$

where $z(l,b)$ is defined via (13). The integral (51) can be thought of as the (normalized) turbulent contribution into the overall STEC defined similar to (14):

$$\text{STEC}(b;z_0,l_0) = \int_{\text{RaySgmnt}(b;z_0,l_0)} N_T(z,h)\,d\ell.$$

In Section IV-B, we will associate the numerator of the right-hand side of (50) with the second exponent in (17).

For simplicity, assume that the baseline ionosphere described by N_e is horizontally homogeneous. Under the assumption (45) and with the normalization as in (51), we have

$$\langle\tilde\varphi^2(b)\rangle = \text{const}(b).$$

The quantity $S_{\tilde\varphi}$ introduced in (50) is called the structure function. It is related to the autocorrelation function $R_{\tilde\varphi}$ via

$$\begin{aligned}S_{\tilde\varphi}(b) &= 2\langle\tilde\varphi^2\rangle - 2\langle\tilde\varphi(0)\tilde\varphi(b)\rangle\\ &= 2\langle\tilde\varphi^2\rangle\left(1 - \frac{\langle\tilde\varphi(0)\tilde\varphi(b)\rangle}{\langle\tilde\varphi^2\rangle}\right)\\ &= 2\langle\tilde\varphi^2\rangle\big(1 - R_{\tilde\varphi}(b)\big)\end{aligned} \tag{52}$$

where

$$\begin{aligned}R_{\tilde\varphi}(b) &= \frac{\langle\tilde\varphi(0)\tilde\varphi(b)\rangle}{\langle\tilde\varphi^2\rangle} = \frac{1}{\langle\tilde\varphi^2\rangle}\left(\frac{4\pi e^2}{m_e\omega_0^2}\right)^2\\ &\quad\cdot\int_0^R dl'\int_0^R dl''\,\big\langle\mu\big(0,l'\big)\mu\big(z(l'',b),l''\big)\big\rangle.\end{aligned} \tag{53}$$

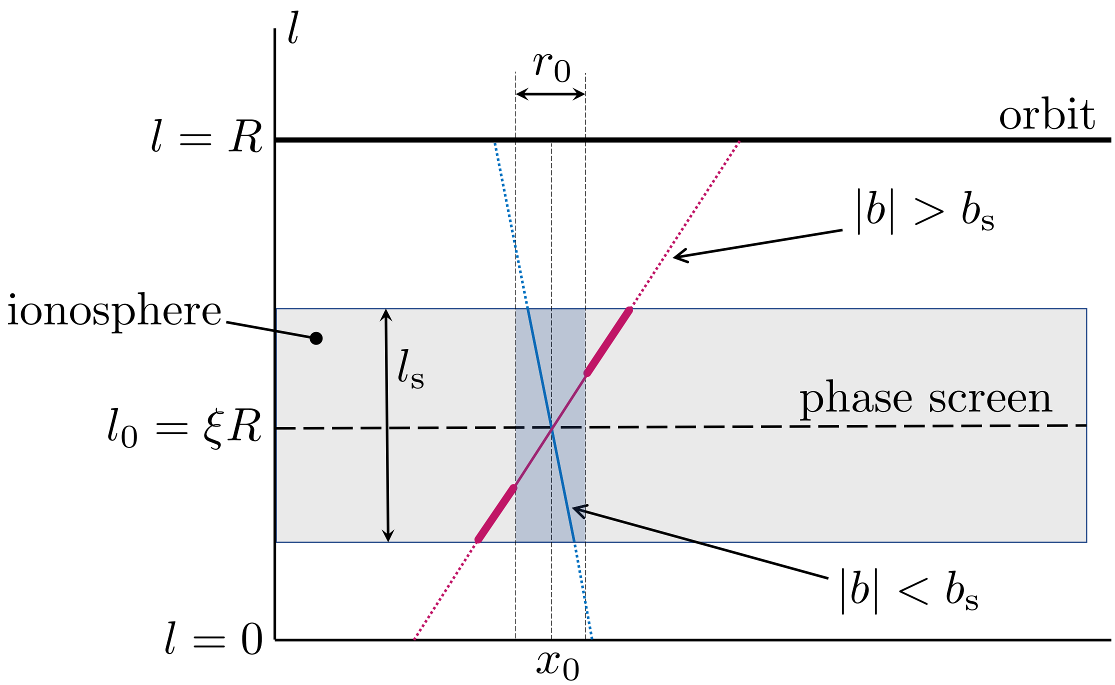

Fig. 2. Geometry of the rays in the slant plane for two different values of the squint parameter b, given the correlation radius r_0 and thickness of the ionosphere $h_s = l_s \cos\theta$ (see Fig. 1). Angles are not to scale.

Unlike in Section III, in this section, we are considering much shorter horizontal scales of ionospheric perturbations than those given by (24). Hence, the polynomial approximation (30) cannot be used to represent the integrand in (53). Instead, we make the following assumption about the autocorrelation function of the turbulent fluctuations (see [10, Ch. 4]):

$$\langle \mu(z', l')\mu(z'', l'')\rangle = V_R\left(\frac{l' + l''}{2}\right) V_r(r) \tag{54}$$

where

$$r = \sqrt{|z'' - z'|^2 + |l'' - l'|^2}.$$

We assume that V_r accounts for the short-range nature of the fluctuations and, thus, decays rapidly on the scale of $r_0 \ll h_s$, where the constant r_0 is called the correlation radius of the medium. Similarly to [10] (see also [53]), it can be shown that in this case

$$\langle\tilde{\varphi}(0)\tilde{\varphi}(b)\rangle \approx \left(\frac{4\pi e^2}{m_e}\right)^2 R \cdot \int_0^1 V_R(uR) V_\rho\big(|b(u - \xi)|R\big)\, \mathrm{d}u$$

where ξ is the relative screen elevation, see (25), and

$$V_\rho(\rho) = \int_{-\infty}^{\infty} V_r\left(\sqrt{\rho^2 + s^2}\right) \mathrm{d}s. \tag{55}$$

Introduce

$$J(b) = \int_0^1 V_R(uR)\left[V_\rho(0) - V_\rho\big(|b(u - \xi)|R\big)\right] \mathrm{d}u$$
$$J_0 = V_\rho(0)\int_0^1 V_R(uR)\, \mathrm{d}u. \tag{56}$$

Then, from formulas (50) and (52), we can find

$$\zeta_{\tilde{\varphi}}(b) = \frac{1}{2}\frac{S_{\tilde{\varphi}}(b)}{\langle\tilde{\varphi}^2(0)\rangle} = 1 - R_{\tilde{\varphi}}(b) = \frac{J(b)}{J_0}. \tag{57}$$

The effect of the ionosphere of a finite thickness as compared with the representation by a phase screen is characterized by formula (57). We will evaluate this effect for two limiting cases illustrated in Fig. 2. These cases are discriminated by the value of the squint angle:

$$|b| \lessgtr b_s, \quad \text{where } b_s = \frac{r_0}{l_s} = \frac{r_0}{h_s/\cos\theta}. \tag{58}$$

The first case, given by $|b| \lesssim b_s$, corresponds to small squints, such that the ionospheric disturbances on the rays passing through the point (x_0, l_0) are highly correlated, i.e., $\zeta_{\tilde{\varphi}}(b) = 1 - R_{\tilde{\varphi}}(b) \ll 1$ [Fig. 2 (blue line)]. The second case is that of large squints ($|b| \gg b_s$, the purple line) where significant parts of the rays are decorrelated, resulting in $\zeta_{\tilde{\varphi}}(b) \sim 1$.

2) Case of a Small Squint: The function $V_\rho(\rho)$ given by (55) inherits the general behavior of the short-range correlation function $V_r(r)$. It attains its maximum value at $\rho = 0$ and then decreases rapidly for the values of its argument ρ that exceed r_0. We can, therefore, see that for all sufficiently small $|b| < b_s$, the quantity $V_\rho(0) - V_\rho\big(|b(u - \xi)|R\big)$ under the first integral in (56) is also small, because for the second argument, we have $|b(u - \xi)|R < r_0$ regardless of the value of u. Consequently, we can write

$$\frac{V_\rho(0) - V_\rho\big(|b(u - \xi)|R\big)}{V_\rho(0)} \ll 1 \tag{59}$$

which allows us to suggest that for all sufficiently small $|b| < b_s$, the quantity $\zeta_{\tilde{\varphi}}(b)$ defined by (57) via (56) is small, and hence, the ionospheric disturbances on the broadside and squinted rays are strongly correlated; see Fig. 2.

The specific calculations supporting this conclusion are conducted in the Appendix, where we find the leading terms of the asymptotic expansion of $\zeta_{\tilde{\varphi}}(b)$ as $b/b_s \to 0$ for two commonly used models of ionospheric turbulence: Gaussian turbulence and Kolmogorov turbulence. The resulting expressions are as follows [see (90) and (96)]:

$$\zeta_{\tilde{\varphi},G}(b) = Q_G(b/b_s)^2 \quad \text{and } \zeta_{\tilde{\varphi},K}(b) = Q_K(|b|/b_s)^{2\gamma}. \tag{60}$$

In (60), $Q_G \sim 1$ and $Q_K \sim 1$ are constants calculated from the profiles V_R and V_r, see (54), and $\gamma = 5/6$, see (94). For $|b| \ll b_s$, each of the expressions in (60) yields

$$\zeta_{\tilde{\varphi}}(b) \ll 1. \tag{61}$$

3) Case of a Large Squint: Now, we turn to the case opposite to that of Section IV-A2, namely, $|b| > b_s$, as illustrated by the purple ray in Fig. 2. For the integrals in (56), the thick segments indicate the intervals of the values of u, where the expression on the left-hand side of (59) is not small for the corresponding value of b. This means that $\zeta_{\tilde{\varphi}}(b) = 1 - R_{\tilde{\varphi}}(b)$ is not small either.

The effect of a finite thickness of the ionosphere is still given by formulas (56) and (57). However, the analytic integration in (56) appears problematic without further simplifications. To obtain a rough estimate, we will take $V_R(uR) = \text{const}$ for $|uR - l_0|\cos\theta \le h_s/2$, cf. (42). We also replace V_ρ with the indicator function

$$\frac{V_\rho(\rho)}{V_\rho(0)} = \begin{cases} 1, & \text{if } |\rho| \le r_0 \\ 0, & \text{otherwise.} \end{cases} \tag{62}$$

Note that the representation (62) is meaningful for both the Gaussian (Appendix A) and Kolmogorov (Appendix B) turbulence models (see [10, Appendix 4.A]). With these simplifications, the fraction $J(b)/J_0$ on the right-hand side of (57) can be interpreted as the ratio of the length of two thick purple segments, see Fig. 2, to the overall length of the ray within the ionospheric layer (i.e., thick and thin solid segments combined). Note that with the model (62), the decorrelated segments exist only for $|b| \gtrsim r_0/l_s = b_s$. Using the similarity of the triangles, we can obtain

$$\zeta_{\tilde{\varphi}}(b) \sim 1 - \frac{r_0}{bl_s} \equiv 1 - \frac{b_s}{|b|}. \tag{63}$$

As the thickness of the ionosphere increases and/or the squint of the ray becomes larger, the value of $\zeta_{\tilde{\varphi}}(b)$ given by (63) for $b \neq 0$ increases and approaches one, as expected.

According to the definition of the metric $\zeta_{\tilde{\varphi}}$ in (50), $\zeta_{\tilde{\varphi}}(b) \sim 1$ means that when $|b| \gtrsim b_s$, the differences between the perturbations of the eikonal modeled by the phase screen and the ionosphere having a finite thickness are, on average, significant (i.e., comparable to the magnitude of the baseline perturbations).

B. Statistics of Eikonals for the Rays Associated With a Single Image Point

In Section IV-A, we considered the statistics of eikonals for the rays passing through one and the same point on the phase screen. We have used the parameter $\zeta_{\tilde{\varphi}}(b)$, see (50), as a measure of decorrelation between the normalized eikonals $\tilde{\varphi}$ for the ray with the squint parameter b and that for the corresponding broadside ray. For the analysis of imaging with the correction term, we will need to obtain the statistical properties of the sum (17). That, in turn, requires knowing the statistics of the variable $\phi(x, y)$ defined in (48) as follows:

$$\phi(x, y) = \varphi(x, y) - \varphi^{\text{rec}}(x, y)$$

where y is the image coordinate.

When the correction term is implemented using a phase screen, see (17) with (21), we identify $\varphi(x, y)$ and $\varphi^{\text{rec}}(x, y)$ with $\tilde{\varphi}(b)$ and $\tilde{\varphi}(0)$ in (50), respectively, given that

$$z_0 = s(x, y) = \xi x + (1 - \xi)y \quad \text{and } l_0 = \xi R$$

see also (21), (27), and (51). We will express the statistics of $\phi(x, y)$ via the results of Section IV-A with

$$b = \frac{x - y}{R} \tag{64}$$

see Fig. 1. In doing so, we will ignore the difference between $\varphi(b)$ and $\tilde{\varphi}(b)$, see (51), since $|b| \le L_{\text{SA}}/(2R)$ and typically $L_{\text{SA}} \ll R$, which results in $(1 + b^2)^{1/2} - 1 \ll 1$. Thus, similar to $\zeta_{\tilde{\varphi}}(b)$ in (50), we introduce $\zeta(x, y)$ as follows:

$$\begin{aligned} \left\langle \left(\phi(x, y)\right)^2 \right\rangle &= \left\langle \left(\varphi(x, y) - \varphi^{\text{rec}}(x, y)\right)^2 \right\rangle \\ &= 2\langle \varphi^2 \rangle \zeta(x, y). \end{aligned} \tag{65}$$

Note that while some antenna coordinates x_j in the sum in (17) correspond to the small-squint case, others may yield the rays with large squint if the SA is large enough. In order to analyze the resulting sum, we have to combine the approximations (60), (61), and (63). Given that (63) is a rough estimate, and taking into account that the parameter $b_s = r_0/l_s$ characterizes both the size of the domain where inequality (61) holds and the scale of the argument b in (63), we perform a further simplification and present the unifying approximation to $\zeta_{\tilde{\varphi}}(x, y)$ in the following form:

$$\zeta(x, y) \approx \zeta_b(b) = \begin{cases} 0, & \text{if } |b| \le b_s \\ 1 - b_s/|b|, & \text{otherwise} \end{cases} \tag{66}$$

where b is related to x and y by (64).

To calculate the statistical characteristics of the imaging kernel (17), we use the central limit theorem and also employ the clustering approximation introduced in [54] (see also [2], [10, Sec. 4.3], [53]). According to the central limit theorem, each perturbation $\varphi = \varphi(x, y)$ can be considered a Gaussian random variable with zero mean [19, Ch. I], because the integration path (ray) crosses through many identically distributed turbulent inhomogeneities. In addition, we assume that the synthetic array is partitioned into a set of nonintersecting clusters, such that the eikonals φ that belong to the same cluster are strongly correlated and thus (nearly) identical, while those that belong to different clusters are uncorrelated and, therefore, independent. The same assumptions extend to the reconstruction term φ^{rec} defined via (21) and (27) and, accordingly, the difference $\phi = \varphi - \varphi^{\text{rec}}$ in (17). The length of the cluster L_c and the cluster index m for the antenna location x_j will be defined as follows:

$$L_c = \frac{r_0}{\xi}, \quad m = \left[\frac{x_j - y}{L_c}\right] \tag{67}$$

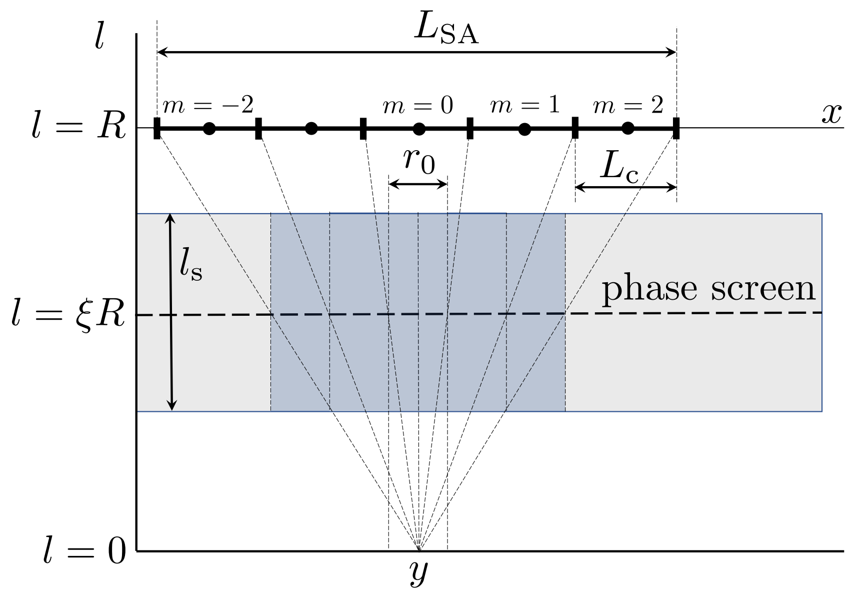

Fig. 3. Approximate approach for computing the eikonal correlation function using clusters; see (68) and (70). To illustrate the idea, we show the total number of clusters as equal to 5, with the cluster indices from $m = -2$ to $m = 2$. The small black bars indicate the cluster boundaries, i.e., $x_m^\pm$ given by (73) (assuming that $|y - z| \ll L_c$), while the filled circles between them correspond to $x(y, m)$; see (71). Angles are not to scale.

where $[\cdot]$ denotes rounding to the nearest integer; see Fig. 3. Using m and m' as cluster indices corresponding to the antenna locations x_j and $x_{j'}$, respectively, we, thus, have

$$\frac{1}{2}k^2\langle\phi(x_j, y)\phi(x_{j'}, y)\rangle = \frac{1}{2}k^2\langle\phi(x_j, y)^2\rangle\delta_{mm'} \stackrel{\rm def}{=} \mathcal{D}_m^2\delta_{mm'} \quad (68)$$

where

$$\mathcal{D}_m^2 = 2\mathcal{D}^2\zeta_b\left(\frac{L_c}{R}m\right) \quad (69)$$

see (49) and (64)–(67).

In Section IV-C, we analyze the SAR imaging with kernel (17), where the statistics of phase perturbations are described by (65)–(69).

C. Imaging Through a Turbulent Ionosphere With Corrections Realized by a Phase Screen

The clustering assumption of Section IV-B allows us to split the sum in (17) into clusterwise terms V_m and factor out the random exponentials containing ϕ_m, with m being the cluster index:

$$W(y, z) = \sum_m V_m(y, z) = \sum_m U_m(y, z)\exp(-ik\phi_m) \quad (70)$$

where, according to (67)

$$\phi_m = \varphi\big(x(y, m), y\big) - \varphi^{\rm rec}\big(x(y, m), y\big) \quad (71)$$

and $x(y, m) = y + mL_c$. In (70), the terms U_m are deterministic and can be written as follows:

$$U_m = \frac{1}{N}\sum_{x_m^- \le x_j < x_m^+}\exp\left[2ik\frac{y-z}{R}\left(x_j - \frac{y+z}{2}\right)\right] \quad (72)$$

where the cluster boundaries are given by

$$x_m^- = \frac{y+z}{2} + \left(m - \frac{1}{2}\right)L_c, \quad x_m^+ = \frac{y+z}{2} + \left(m + \frac{1}{2}\right)L_c. \quad (73)$$

Assuming that the distance between the successive antenna positions is sufficiently small, we approximate the sum in (72) by an integral and obtain

$$U_m = \frac{L_c}{L_{\rm SA}}\exp(2im\eta)\frac{\sin\eta}{\eta} \equiv \frac{L_c}{L_{\rm SA}}\exp(2im\eta)\,{\rm sinc}\,\eta \quad (74)$$

where

$$\eta = \frac{kL_c(y-z)}{R}. \quad (75)$$

Note that the width of the main lobe of the sinc function in (74) corresponds to unperturbed imaging with $L_{\rm SA} = L_c$; see (19) and (20).

Proceeding to the statistical characteristics of $W(y, z)$ given by (70), we make use of the fact that ϕ_m for different values of m are independent and Gaussian; see (68) and the preceding discussion. With the help of (68) and (74), we obtain the following expressions for the mean of $W(y, z)$:

$$\begin{aligned}\langle W(y, z)\rangle &= \sum_m\langle V_m(y, z)\rangle \\ &= \sum_m U_m(y, z)\langle\exp(-ik\phi_m)\rangle \\ &= \sum_m U_m(y, z)\exp\left(-\mathcal{D}_m^2\right) \\ &= \frac{L_c}{L_{\rm SA}}\,{\rm sinc}\,\eta\sum_m\exp(2im\eta)\exp\left(-\mathcal{D}_m^2\right)\end{aligned} \quad (76)$$

while for the variance of $W(y, z)$, we have

$${\rm Var}\,W(\eta) = \left\langle|W(y, z) - \langle W(y, z)\rangle|^2\right\rangle$$

$$= \sum_m \left\langle |V_m(y,z) - \langle V_m(y,z)\rangle|^2 \right\rangle$$
$$= \sum_m |U_m(y,z)|^2 \left\langle |\exp(-ik\phi_m) - \langle \exp(-ik\phi_m)\rangle|^2 \right\rangle$$
$$= \left(\frac{L_c}{L_{\mathrm{SA}}} \operatorname{sinc} \eta\right)^2 \sum_m \left[1 - \exp\left(-2\mathcal{D}_m^2\right)\right] \tag{77}$$

see [54]. It can be shown that as $\mathcal{D}^2 \to 0$, the mean PSF given by (76) converges to the unperturbed expression (19), i.e.,

$$\langle W(\eta)\rangle \to W_{\lim}(\eta) = \operatorname{sinc}\left(\frac{L_{\mathrm{SA}}}{L_c}\eta\right) \equiv \operatorname{sinc}\left(\frac{kL_{\mathrm{SA}}(y-z)}{R}\right) \tag{78}$$

while the variance given by (77) vanishes.

A commonly used metric for assessing the sharpness of the image due to a point scatterer is the integrated sidelobe ratio (ISLR). We will define it here using the operators Peak[·] and SL[·] that single out the peak and sidelobes, respectively, in the PSF. For the deterministic PSF $W_{\lim}$ given by (78), we assign the peak boundary to the first zero of the sinc function:

$$\eta_0 = \pi L_c / L_{\mathrm{SA}} \tag{79}$$

so that

$$\mathrm{Peak}[W_{\lim}](\eta) = \begin{cases} W_{\lim}(\eta), & \text{if } |\eta| \le \eta_0 \\ 0, & \text{otherwise} \end{cases}$$
$$\mathrm{SL}[W_{\lim}](\eta) = \begin{cases} W_{\lim}(\eta), & \text{if } \quad |\eta| > \eta_0 \\ 0, & \text{otherwise.} \end{cases} \tag{80}$$

ISLR is then defined as in [48, Sec. 2.8]:

$$\mathrm{ISLR}(W) = 10\log_{10}\frac{\|\mathrm{SL}[W]\|^2}{\|\mathrm{Peak}[W]\|^2} \tag{81}$$

where

$$\|F\|^2 \equiv \|F(\eta)\|^2 = \int_{-\infty}^{\infty} |F(\eta)|^2 \, d\eta$$

which yields $\mathrm{ISLR}(W_{\lim}) \approx -9.68$ dB (see [10, footnote 16, p. 260]). Other considerations can be employed to identify the peak, thus affecting the value of ISLR. For example, if we define η_0 in (80) using the so-called "3-dB rule," see [48, Sec. 2.3.4], i.e., implicitly by $|W(\eta_0)| = |W(0)| \times 10^{-0.3} \approx |W(0)| \times 0.5$; then, we obtain $\mathrm{ISLR}(W_{\lim}) \approx -13$ dB.

In the case where the magnitude of phase fluctuations is large, defining the peak boundary with the help of the unperturbed PSF as in (80) and computing the ISLR according to (81) are no longer sufficient. We, therefore, modify the definitions in (79)–(81) to accommodate a large variance of W. First, we introduce a new deterministic function

$$W_S(\eta) = \max\left(|\langle W(\eta)\rangle|, [\mathrm{Var}\, W(\eta)]^{1/2}\right) \tag{82}$$

(note that unlike $W(\eta)$, function $W_S(\eta)$ is always nonnegative). Then, we redefine the peak boundary as the transition point where the variance becomes equal to the mean PSF squared:

$$\eta_{0S} = \min\{|\eta| \mid W_S(\eta) = [\mathrm{Var}\, W(\eta)]^{1/2}\}. \tag{83}$$

For η_{0S} defined by (83), we always have $\eta_{0S} \le \eta_0$ where η_0 is the peak boundary for the deterministic case; see (79) and Fig. 4. In turn, W_S and η_{0S} replace $W_{\lim}$ and η_0 in (80), yielding the statistical versions of the corresponding operators

$$\mathrm{Peak}_S[W](\eta) = \begin{cases} W_S(\eta), & \text{if } |\eta| \le \eta_{0S} \\ 0, & \text{otherwise} \end{cases}$$
$$\mathrm{SL}_S[W](\eta) = \begin{cases} W_S(\eta), & \text{if } \quad |\eta| > \eta_{0S} \\ 0, & \text{otherwise.} \end{cases}$$

Finally, the statistical version of ISLR is defined similar to (81) with these new operators:

$$\mathrm{ISLR}_S(W) = 10\log_{10}\frac{\|\mathrm{SL}_S[W]\|^2}{\|\mathrm{Peak}_S[W]\|^2}. \tag{84}$$

While the mean and variance of W are declared as the functions of η in (76) and (77), they also depend on many other parameters, such as the turbulence level $\mathcal{D}^2$ and the number of clusters in the SA $n_c = L_{\mathrm{SA}}/L_c$. This means that W_S given by (82) depends on the same parameters, and so do all the quantities derived from W_S, including ISLR_S in (84).

Fig. 4 displays the mean and variance of the PSF given by (70) for two distinct values of $\mathcal{D}^2$ with $n_c = 9$. For $\mathcal{D}^2 = 0.1$, we have $\langle W(\eta)\rangle \approx W_{\lim}(\eta)$ and $\mathrm{ISLR}_S(W) \approx -7.81$ dB; the latter value is comparable to the aforementioned unperturbed case characterized by $\mathrm{ISLR}(W_{\lim}) = -9.68$ dB. The situation is different for $\mathcal{D}^2 = 0.8$ where the peak of $\langle W\rangle$ is noticeably lower and variance higher than in the deterministic case. Accordingly, we have $\mathrm{ISLR}_S(W) \approx 0.90$ dB, which is a significantly higher value than that for $\mathcal{D}^2 = 0.1$.

Fig. 5 presents the plots of ISLR_S versus $\mathcal{D}^2$ and n_c. We see that a combination of high level of perturbations and large SA (i.e., $k^2\langle\varphi^2\rangle \sim 1$ and $n_c = L_{\mathrm{SA}}/L_c \gg 1$) results in a high level of sidelobes, leading to a poor imaging performance. Indeed, while for the cluster with $m = 0$, the distortions can be essentially eliminated by the proper choice of the screen density function φ_S, see (66) and (69), the off-center clusters are characterized by larger values of $|b|$ and, hence, will be affected by the phase perturbations; see Figs. 2 and 3. Revisiting formula (17), we can see that in the perturbation-free case, the dependence of W on $(y - z)$ is realized via the first complex exponential under the sum. If the perturbations are present and $k^2\langle\phi^2\rangle \sim \pi$, then there is also the second complex exponential that is random and spread over the entire unit circle. This destroys the information about $(y-z)$ present in the first exponent. Hence, the terms in the sum in (17) with $k^2\langle\phi^2\rangle \sim \pi$ are harmful rather than useful for imaging, because they contribute noise without improving the resolution. In practical settings, it will then be reasonable to throw away the outermost terms in the sum in (12), thus reducing the range of m in (70). Using an appropriate metric, such as ISLR_S, we can determine the optimal length of the SA given the characteristics of perturbations (i.e., $\mathcal{D}^2$ and r_0) and the desired level of sidelobes. For example, if we set the upper bound of admissible ISLR_S at -5 dB, then we can use an SA containing seven clusters as long as $\mathcal{D}^2 \le 0.3$, as indicated by the purple curves on both panels in Fig. 5.

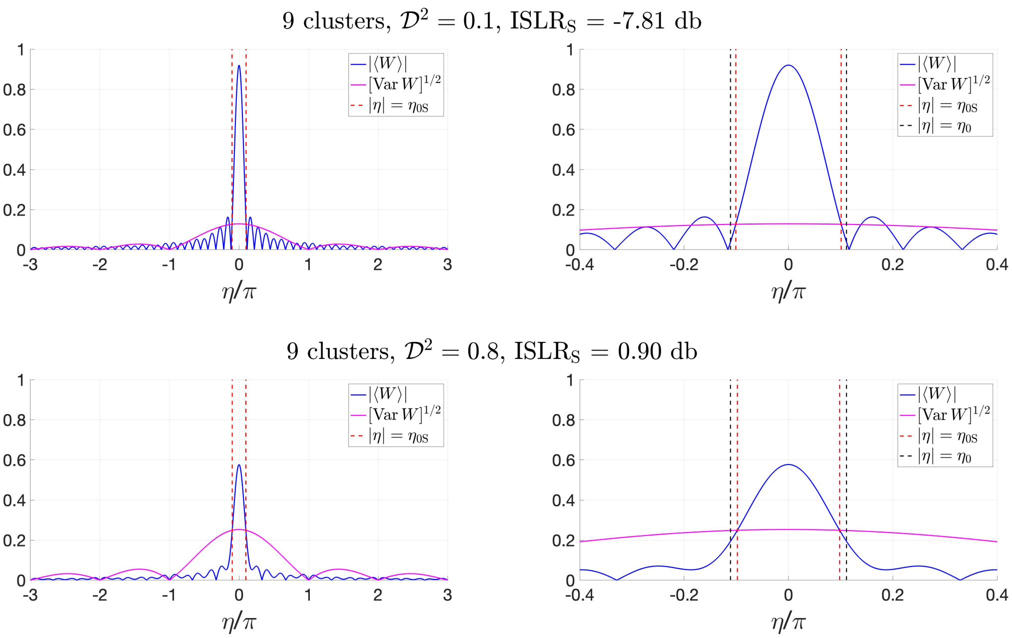

Fig. 4. Left panels: plots of mean and variance of $W(\eta)$ given by (70), with η defined in (75). Right panels: zoomed-in views to the central part of the corresponding left panels. The blue, purple, red, and black lines correspond to formulas (76), (77), (79), and (83), respectively.

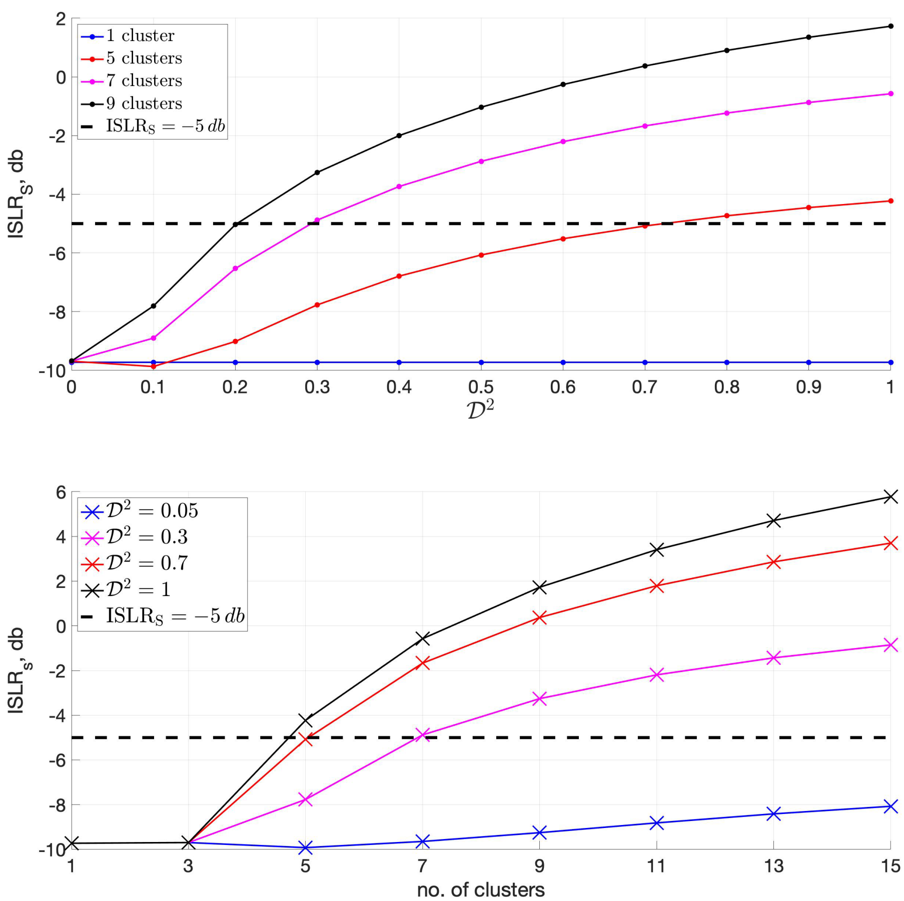

Fig. 5. Plots of ISLR_S versus $\mathcal{D}^2$ and n_c (top and bottom panels, respectively).

If the value of $\mathcal{D}^2$ is higher, say $\mathcal{D}^2 = 0.7$, then we should trim the SA down to five clusters (red curves). The increase of the resolution size resulting from this adjustment, see (20), represents a compromise between the resolution and level of sidelobes in the imaging kernel in the presence of phase noise.

V. Conclusion

For the phase perturbations of radar signals propagating through the Earth's ionosphere, we have studied the efficiency of having a finite-thickness ionosphere represented by means of an infinitesimally thin phase screen. We judged the efficiency in the framework of spaceborne SAR imaging, as the phase screen model was applied to compensate the phase perturbations due to the ionosphere. The resulting image quality was assessed by analyzing the properties of the imaging kernel (the PSF).

For the case of large-scale perturbations considered in Section III, we have found that an efficient compensation of distortions is achievable; i.e., with a proper choice of the phase screen parameters, the resulting image will have very small distortions.

For the opposite case of small-scale perturbations due to the ionospheric turbulence, see Section IV, our findings are different. We have shown that a high level of phase distortions imposes an effective upper limit on the length of the useful part of SA for the corrected image given by formula (12). The optimal length of the SA can be determined by the balance between the improvement of resolution, see (79), and increase of noise due to decorrelation between the actual eikonals and those represented by the phase screen as the SA length increases; see formulas (66)–(69).

For the analysis in this work, we used a mathematical model of the ionosphere. Next, one could ask how accurately a phase screen will represent the perturbations of SAR signals due to the propagation through a real ionosphere. The pertinent accuracy can be assessed by analyzing the distortions of the true ionospheric PSF. The latter, in turn, is obtained by imaging a bright point scatterer, such as a corner reflector. An example of the corresponding study has been reported in [55] and [56].

However, the very definition of a phase screen for the actual ionosphere requires attention. One cannot use formula (47) for the turbulent contribution to the eikonal, because the turbulent part of the electron number density μ cannot be considered known. Indeed, while several methods are available for obtaining the part of the TEC due to the mean electron number density N_e (in particular, dual-carrier probing, see [1], [10, Ch. 3], [40], [54]), those methods do not apply to μ.

In this paper, we do not discuss how to construct a phase screen in the case of an unknown ionosphere. We rather assess the accuracy of representing the corrections to SAR imaging functional by means of a phase screen if the ionosphere is known. Thus, we identify the scenarios where the use of the phase screens is justified. These scenarios are characterized in terms of the relevant parameters of the SAR instrument and the ionosphere and apply to the real ionosphere as well. Subsequently, a phase screen for correcting the ionospheric perturbations can actually be built with the help of special algorithms, such as the transionospheric autofocus [11] (see also [22]).

One of the potential extensions of this work is the concept of a vector-valued phase screen. Besides the value of the broadside eikonal at each point, see (27), this vector may contain values that encode the vertical structure of the plasma layer, e.g., the vertical and/or mixed derivatives of the electron number density. This model may be considered as an alternative to a representation of the ionosphere using multiple phase screens.

Other extensions may include replacing the geometrical optics with a more versatile electromagnetic model, e.g., the parabolic wave equation (PWE) [19], [32], that would, in particular, be capable of describing the amplitude scintillation. Examples of using the phase screens with PWE can be found, e.g., in [57] and [58]. Such constructs open a pathway to analyzing the effect of azimuthal striping (see Section I). Yet to do so, one will also need to take into account the inhomogeneity of the medium across the slant plane. Hence, the 1-D analysis of Section IV shall be generalized to include the range coordinate.

Appendix

We compute the leading term of the decorrelation metric $\zeta_{\tilde{\varphi}}(b)$ given by (57) as $b/b_s \to 0$ for two common models used to describe the ionospheric turbulence: Gaussian turbulence and Kolmogorov turbulence.

A. Gaussian Turbulence

The perturbations of the electron number density due to the Gaussian turbulence are modeled by the following autocorrelation function:

$$V_r(r) = \exp\left(-q_G^2 r^2\right). \tag{85}$$

With the correlation radius r_0 defined by

$$r_0 = \frac{1}{V_r(0)} \int_0^\infty V_r(r)\,\mathrm{d}r \tag{86}$$

we can find that

$$q_G = \frac{\sqrt{\pi}}{2}\frac{1}{r_0} \approx 0.88\frac{1}{r_0}. \tag{87}$$

Formulas (55) and (85) yield

$$V_{\rho,G}(\rho) = 2r_0 \exp\left(-q_G^2 \rho^2\right)$$

and using the Taylor expansion for $\rho \ll r_0$, we can find the leading term of (59) as follows:

$$V_{\rho,G}(0) - V_{\rho,G}(\rho) \approx 2r_0 q_G^2 \rho^2.$$

Hence, for the Gaussian turbulence, formula (57) becomes

$$\zeta_{\tilde{\varphi},G}(b) = (bq_G R)^2 \left(\int_0^1 V_R(uR)(u-\xi)^2\,\mathrm{d}u\right) \cdot \left(\int_0^1 V_R(uR)\,\mathrm{d}u\right)^{-1}. \tag{88}$$

We proceed by choosing a simple "boxcar" model for V_R

$$V_R(l) = \begin{cases} V_0, & \text{if} \quad |l - \xi R| \le h_s/2 \\ 0, & \text{otherwise} \end{cases} \tag{89}$$

where $V_0 = \text{const}$. This allows us to evaluate the integrals in (88), which yields

$$\zeta_{\tilde{\varphi},G}(b) = Q_G \left(\frac{b}{b_s}\right)^2 \tag{90}$$

where b_s is defined in (58) and $Q_G = \pi/48 \approx 0.07$. If $V_R(l)$ is different from (89) while all other assumptions hold, then expression (90) remains valid with $Q_G \sim 1$.

Formula (90) [see also (60)] yields the leading term of the metric describing the accuracy of modeling a "thick" ionosphere by means of a phase screen in the case of a Gaussian turbulence as $b/b_s \to 0$. The factor $(b/b_s)^2$ on the right-hand side of formula (90) guarantees that $\zeta_{\tilde{\varphi},G}(b) \ll 1$ if $|b| \ll b_s$. According to (50), this means that the perturbations of the eikonal due to the "thick" ionosphere can be relatively well represented by a properly chosen phase screen.

B. Kolmogorov Turbulence

For the Kolmogorov turbulence, the perturbations are defined via their (spatial) spectrum

$$\hat{V}_r(\boldsymbol{q}) = \frac{C}{\left(1 + (|\boldsymbol{q}|^2/q_K^2)\right)^{\kappa}} \tag{91}$$

where

$$\kappa = \frac{11}{6}, \quad C = \frac{\Gamma(\kappa)}{\pi^{3/2} q_K^3 \Gamma\left(\kappa - (3/2)\right)}$$

see [10, Sec. 4.A.4]. From (86), we can obtain [see (87)]

$$q_K = \frac{\sqrt{\pi}\,\Gamma(\kappa)}{(\kappa - 1)\Gamma\left(\kappa - (3/2)\right)} \frac{1}{r_0} \approx 0.75 \frac{1}{r_0}.$$

We can derive V_r by the inverse Fourier transform of $\hat{V}_r(\boldsymbol{q})$ given by (91)[5] and substitute the result into (55), which yields

$$V_{\rho,K}(\rho) = \frac{1}{q_K} \frac{2^{3-\gamma}\sqrt{\pi}\,\Gamma\left(\kappa - (3/2)\right)}{\Gamma\left(\kappa - (3/2)\right)} (q_K \rho)^{\gamma} K_{\gamma}(q_K \rho) \tag{92}$$

where $\gamma = \kappa - 1$ and K_γ is the Macdonald function, or modified Bessel function of the second kind (see [59, Ch. 10]). The function $\eta^\gamma K_\gamma(\eta)$ is not twice differentiable at $\eta = 0$, and its asymptotic behavior near zero is given by the first two terms of the Puiseux series[6]

$$\eta^{\gamma} K_{\gamma}(\eta) \approx 2^{\gamma-1}\Gamma(\gamma)\left(1 + \frac{\Gamma(-\gamma)}{2^{\gamma}\Gamma(\gamma)}|\eta|^{2\gamma}\right) \tag{93}$$

where

$$2\gamma = 2(\kappa - 1) = \frac{5}{3}. \tag{94}$$

Since $0 < \gamma < 1$, we have $\Gamma(\gamma) > 0$, and $\Gamma(-\gamma) < 0$. Consequently, the function defined by formula (93) attains a maximum at $\eta = 0$, which is consistent with the standard properties of an autocorrelation function $R_{\tilde{\varphi}}$. Indeed, if $\eta = 0$ were to deliver a minimum rather than a maximum to (93), then the first integral in (56) and, hence, the right-hand side of (57) could become negative, which would allow $R_{\tilde{\varphi}} > 1$. This, however, is not possible, since $R_{\tilde{\varphi}}$ is an autocorrelation function.

[5]For a spatially inhomogeneous random process μ, the formulation in (91) assumes that V_R in (54) varies on a scale much larger than $r_0 \sim q_K^{-1}$.

[6]The expression on the right-hand side of (93) has been obtained using Wolfram Mathematica®; see [60].

Substituting (92) into (59) and proceeding as in Appendix A, we arrive at

$$\zeta_{\tilde{\varphi},K}(b) = \frac{|\Gamma(-\gamma)|}{2^{\gamma}\Gamma(\gamma)} |b q_K R|^{2\gamma} \left(\int_0^1 V_R(uR)|u - \xi|^{2\gamma}\,\mathrm{d}u\right) \cdot \left(\int_0^1 V_R(uR)\,\mathrm{d}u\right)^{-1}. \tag{95}$$

Similarly to the case of a Gaussian turbulence, we evaluate (95) using the model (89) for $V_R(l)$. The resulting expression for the Kolmogorov-type turbulence is

$$\zeta_{\tilde{\varphi},K}(b) = Q_K \left(\frac{|b|}{b_s}\right)^{2\gamma} \tag{96}$$

where

$$Q_K = \frac{|\Gamma(-\gamma)|}{2^{\gamma}\Gamma(\gamma)} \frac{1}{2^{2\gamma}(2\gamma + 1)} \left(\frac{\sqrt{\pi}\,\Gamma(\kappa)}{(\kappa - 1)\Gamma\left(\kappa - (3/2)\right)}\right)^{2\gamma} \approx 0.2.$$

To accommodate the more general forms of V_R, we assume that $Q_K \sim 1$. Obviously, formula (96) [see also (60)] yields $\zeta_{\tilde{\varphi},K}(b) \ll 1$ for $|b| \ll b_s$. This is also similar to the case of the Gaussian correlation function considered in Appendix A.

Acknowledgment

The authors thank the anonymous referees of this article for their valuable comments and suggestions.

References

[1] M. Gilman, E. Smith, and S. Tsynkov, "Reduction of ionospheric distortions for spaceborne synthetic aperture radar with the help of image registration," *Inverse Problems*, vol. 29, no. 5, May 2013, Art. no. 054005.

[2] M. Gilman and S. Tsynkov, "Mathematical analysis of SAR imaging through a turbulent ionosphere," in *Proc. AIP Conf.*, vol. 1895, M. D. Todorov, Ed., 2017, pp. 1–23.

[3] A. Ishimaru, Y. Kuga, J. Liu, Y. Kim, and T. Freeman, "Ionospheric effects on synthetic aperture radar at 100 MHz to 2 GHz," *Radio Sci.*, vol. 34, no. 1, pp. 257–268, Jan. 1999.

[4] N. A. Armand, "On limitation of the resolution of space born synthetic aperture radars caused by the conditions of radio propagation in ionosphere," *Explor. Earth Space*, no. 1, pp. 27–38, 2005.

[5] D. P. Belcher, "Theoretical limits on SAR imposed by the ionosphere," *IET Radar, Sonar Navigat.*, vol. 2, no. 6, pp. 435–448, Dec. 2008.

[6] F. J. Meyer, "Performance requirements for ionospheric correction of low-frequency SAR data," *IEEE Trans. Geosci. Remote Sens.*, vol. 49, no. 10, pp. 3694–3702, Oct. 2011.

[7] P. A. Rosen, S. Hensley, and C. Chen, "Measurement and mitigation of the ionosphere in L-band interferometric SAR data," in *Proc. IEEE Radar Conf.*, May 2010, pp. 1459–1463.

[8] J. Chen and H. A. Zebker, "Ionospheric artifacts in simultaneous L-band InSAR and GPS observations," *IEEE Trans. Geosci. Remote Sens.*, vol. 50, no. 4, pp. 1227–1239, Apr. 2012.

[9] J. S. Kim, A. Danklmayer, and K. Papathanassiou, "Correction of ionospheric distortions in low frequency interferometric SAR data," in *Proc. IEEE Int. Geosci. Remote Sens. Symp.*, Jul. 2011, pp. 1505–1508.

[10] M. Gilman, E. Smith, and S. Tsynkov, *Transionospheric Synthetic Aperture Imaging* (Applied and Numerical Harmonic Analysis). Cham, Switzerland: Springer, 2017.

[11] M. Gilman and S. V. Tsynkov, "Transionospheric autofocus for synthetic aperture radar," *SIAM J. Imag. Sci.*, vol. 16, no. 4, pp. 2144–2174, Dec. 2023.

[12] F. Meyer, R. Bamler, N. Jakowski, and T. Fritz, "The potential of low-frequency SAR systems for mapping ionospheric TEC distributions," *IEEE Geosci. Remote Sens. Lett.*, vol. 3, no. 4, pp. 560–564, Oct. 2006.

[13] L. Li and F. Li, "Ionosphere tomography based on spaceborne SAR," *Adv. Space Res.*, vol. 42, no. 7, pp. 1187–1193, Oct. 2008.

[14] X. Pi, A. Freeman, B. Chapman, P. Rosen, and Z. Li, "Imaging ionospheric inhomogeneities using spaceborne synthetic aperture radar," *J. Geophys. Res., Space Phys.*, vol. 116, no. A4, pp. 1–13, Apr. 2011.

[15] M. Jehle, O. Frey, D. Small, and E. Meier, "Measurement of ionospheric TEC in spaceborne SAR data," *IEEE Trans. Geosci. Remote Sens.*, vol. 48, no. 6, pp. 2460–2468, Jun. 2010.

[16] X. Pi, "Ionospheric effects on spaceborne synthetic aperture radar and a new capability of imaging the ionosphere from space," *Space Weather*, vol. 13, no. 11, pp. 737–741, Nov. 2015.

[17] N. Blaunstein and E. Plohotniuc, *Ionosphere and Applied Aspects of Radio Communication and Radar*. Boca Raton, FL, USA: CRC Press, 2008.

[18] V. L. Ginzburg, *The Propagation of Electromagnetic Waves in Plasmas* (International Series of Monographs on Electromagnetic Waves). vol. 7. Oxford, U.K.: Pergamon Press, 1964.

[19] S. M. Rytov, Y. A. Kravtsov, and V. I. Tatarskii, *Principles of Statistical Radiophysics. Wave Propagation Through Random Media*, vol. 4. Berlin, Germany: Springer-Verlag, 1989.

[20] K. E. Mattar and A. L. Gray, "Reducing ionospheric electron density errors in satellite radar interferometry applications," *Can. J. Remote Sens.*, vol. 28, no. 4, pp. 593–600, Jan. 2002.

[21] R. Brcic, A. Parizzi, M. Eineder, R. Bamler, and F. Meyer, "Estimation and compensation of ionospheric delay for SAR interferometry," in *Proc. IEEE Int. Geosci. Remote Sens. Symp.*, Jul. 2010, pp. 2908–2911.

[22] M. Gilman and S. Tsynkov, "Vertical autofocus for the phase screen in a turbulent ionosphere," *Inverse Problems*, vol. 39, no. 4, Apr. 2023, Art. no. 045001.

[23] P. A. Wright, S. Quegan, N. S. Wheadon, and C. D. Hall, "Faraday rotation effects on l-band spaceborne SAR data," *IEEE Trans. Geosci. Remote Sens.*, vol. 41, no. 12, pp. 2735–2744, Dec. 2003.

[24] F. J. Meyer and J. B. Nicoll, "Prediction, detection, and correction of Faraday rotation in full-polarimetric L-band SAR data," *IEEE Trans. Geosci. Remote Sens.*, vol. 46, no. 10, pp. 3076–3086, Oct. 2008.

[25] K. Davies and E. K. Smith, "Ionospheric effects on satellite land mobile systems," *IEEE Antennas Propag. Mag.*, vol. 44, no. 6, pp. 24–31, Dec. 2002.

[26] A. Freeman and S. S. Saatchi, "On the detection of Faraday rotation in linearly polarized L-band SAR backscatter signatures," *IEEE Trans. Geosci. Remote Sens.*, vol. 42, no. 8, pp. 1607–1616, Aug. 2004.

[27] J. S. Kim, K. P. Papathanassiou, R. Scheiber, and S. Quegan, "Correcting distortion of polarimetric SAR data induced by ionospheric scintillation," *IEEE Trans. Geosci. Remote Sens.*, vol. 53, no. 12, pp. 6319–6335, Dec. 2015.

[28] V. Gracheva, J. S. Kim, P. Prats-Iraola, R. Scheiber, and M. Rodriguez-Cassola, "Combined estimation of ionospheric effects in SAR images exploiting Faraday rotation and autofocus," *IEEE Geosci. Remote Sens. Lett.*, vol. 19, pp. 1–5, 2022.

[29] M. Gilman and S. Tsynkov, "Differential Faraday rotation and polarimetric SAR," *SIAM J. Appl. Math.*, vol. 78, no. 3, pp. 1422–1449, Jan. 2018.

[30] M. Gilman and S. Tsynkov, "Polarimetric radar interferometry in the presence of differential Faraday rotation," *Inverse Problems*, vol. 38, no. 4, Mar. 2022, Art. no. 045010.

[31] D. P. Belcher and P. S. Cannon, "Amplitude scintillation effects on SAR," *IET Radar, Sonar Navigat.*, vol. 8, no. 6, pp. 658–666, Jul. 2014.

[32] D. Vasylyev, Y. Béniguel, W. Volker, M. Kriegel, and J. Berdermann, "Modeling of ionospheric scintillation," *J. Space Weather Space Climate*, vol. 12, p. 22, Jan. 2022.

[33] S. Mohanty, G. Singh, C. S. Carrano, and S. Sripathi, "Ionospheric scintillation observation using space-borne synthetic aperture radar data," *Radio Sci.*, vol. 53, no. 10, pp. 1187–1202, Oct. 2018.

[34] J. S. Kim, K. P. Papathanassiou, H. Sato, and S. Quegan, "Detection and estimation of equatorial spread F scintillations using synthetic aperture radar," *IEEE Trans. Geosci. Remote Sens.*, vol. 55, no. 12, pp. 6713–6725, Dec. 2017.

[35] H. Sato, J. S. Kim, Y. Otsuka, C. M. Wrasse, E. Rodrigues de Paula, and J. R. de Souza, "L-band synthetic aperture radar observation of ionospheric density irregularities at equatorial plasma depletion region," *Geophys. Res. Lett.*, vol. 48, no. 16, Aug. 2021, Art. no. e2021GL093541.

[36] H. Kil, "The morphology of equatorial plasma bubbles—A review," *J. Astron. Space Sci.*, vol. 32, no. 1, pp. 13–19, Mar. 2015.

[37] A. Bhattacharyya, "Equatorial plasma bubbles: A review," *Atmosphere*, vol. 13, no. 10, p. 1637, Oct. 2022.

[38] V. Charles et al., *Spotlight-Mode Synthetic Aperture Radar*. Cham, Switzerland: Springer, 1996.

[39] M. Cheney and B. Borden, *Fundamentals of Radar Imaging, Volume 79 of CBMS-NSF Regional Conference Series in Applied Mathematics*. Philadelphia, PA, USA: SIAM, 2009.

[40] E. M. Smith and S. V. Tsynkov, "Dual carrier probing for spaceborne SAR imaging," *SIAM J. Imag. Sci.*, vol. 4, no. 2, pp. 501–542, Jan. 2011.

[41] R. Brcic, A. Parizzi, M. Eineder, R. Bamler, and F. Meyer, "Ionospheric effects in SAR interferometry: An analysis and comparison of methods for their estimation," in *Proc. IEEE Int. Geosci. Remote Sens. Symp.*, Vancouver, BC, Canada, Jul. 2011, pp. 1497–1500.

[42] T. D. Damon and F. R. Hartranft, "Ionospheric electron density profile model," Aerosp. Environ. Support Center, USAF Air Weather Service, 4th Weather Wing, Ent AFB, CO, USA, Tech. Memorandum 70-3, 1970.

[43] S. M. Stankov, K. Stegen, P. Muhtarov, and R. Warnant, "Local ionospheric electron density profile reconstruction in real time from simultaneous ground-based GNSS and ionosonde measurements," *Adv. Space Res.*, vol. 47, no. 7, pp. 1172–1180, Apr. 2011.

[44] K. Hocke and K. Schlegel, "A review of atmospheric gravity waves and travelling ionospheric disturbances: 1982–1995," *Annales Geophysicae*, vol. 14, no. 9, pp. 917–940, Sep. 1996.

[45] K. C. Yeh and C. H. Liu, "Diagnosis of the turbulent state of ionospheric plasma by propagation methods," *Radio Sci.*, vol. 12, no. 6, pp. 1031–1034, Nov. 1977.

[46] P. L. Dyson, J. P. McClure, and W. B. Hanson, "In situ measurements of the spectral characteristics ofFregion ionospheric irregularities," *J. Geophys. Res.*, vol. 79, no. 10, pp. 1497–1502, Apr. 1974.

[47] *Real-Time Ionospheric Maps*. Accessed: Nov. 27, 2023. [Online]. Available: https://iono.jpl.nasa.gov

[48] I. G. Cumming and F. H. Wong, *Digital Processing of Synthetic Aperture Radar Data. Algorithms and Implementation*. Boston, MA, USA: Artech House, 2005.

[49] C. Musgrove and R. Naething, "A method to evaluate residual phase error for polar formatted synthetic aperture radar systems," *Proc. SPIE*, vol. 8714, pp. 361–370, Oct. 2013.

[50] C. Wang, M. Zhang, Z.-W. Xu, C. Chen, and L.-X. Guo, "Cubic phase distortion and irregular degradation on SAR imaging due to the ionosphere," *IEEE Trans. Geosci. Remote Sens.*, vol. 53, no. 6, pp. 3442–3451, Jun. 2015.

[51] G. Kirchengast, K. Hocke, and K. Schlegel, "Gravity waves determined by modeling of traveling ionospheric disturbances in incoherent-scatter radar measurements," *Radio Sci.*, vol. 30, no. 5, pp. 1551–1567, Sep. 1995.

[52] F. J. Meyer, "Quantifying ionosphere-induced image distortions in L-band SAR data using the ionospheric scintillation model WBMOD," in *Proc. 10th Eur. Conf. Synth. Aperture Radar*, Jun. 2014, pp. 1–4.

[53] J. Garnier and K. Sølna, "A multiscale approach to a synthetic aperture radar in dispersive random media," *Inverse Problems*, vol. 29, no. 5, May 2013, Art. no. 054006.

[54] S. V. Tsynkov, "On SAR imaging through the earth's ionosphere," *SIAM J. Imag. Sci.*, vol. 2, no. 1, pp. 140–182, Jan. 2009.

[55] C. R. Mannix, D. P. Belcher, and P. S. Cannon, "Measurement of ionospheric scintillation parameters from SAR images using corner reflectors," *IEEE Trans. Geosci. Remote Sens.*, vol. 55, no. 12, pp. 6695–6702, Dec. 2017.

[56] C. R. Mannix, "Measuring and modelling the impact of the ionosphere on space based synthetic aperture radars," Ph.D. thesis, School Eng., College Eng. Phys. Sci., Univ. Birmingham, Birmingham, U.K., 2016.

[57] V. Fabbro and L. Feral, "Comparison of 2D and 3D electromagnetic approaches to predict tropospheric turbulence effects in clear sky conditions," *IEEE Trans. Antennas Propag.*, vol. 60, no. 9, pp. 4398–4407, Sep. 2012.

[58] S. Mukherjee and C. Yardim, "Accurate computation of scintillation in tropospheric turbulence with parabolic wave equation," *IEEE Trans. Antennas Propag.*, vol. 69, no. 8, pp. 4748–4757, Aug. 2021.

[59] F. W. J. Olver. *NIST Digital Library of Mathematical Functions*. Accessed: Nov. 27, 2023. [Online]. Available: http://dlmf.nist.gov/

[60] *Mathematica, Version 13.2*, Wolfram Research, Inc., Champaign, IL, USA, 2022.